Chalcopyrite Crystals Doped with Transition Elements and Rare Earths

Katsuaki SATO

Department of Applied Physics, Tokyo University of Agriculture and Technology,
Koganei, Tokyo 184-8588, Japan

Transition atom (TA) impurities have been known to introduce characteristic absorptions in I-III-VI$_2$ chalcopyrite type semiconductors. These spectra have been interpreted in terms of intrasystem optical transitions in the 3d^n or 4f^n configuration of TA ions or charge transfer type transitions between the TA orbitals and host band states. Recently Mn, one of the TA atoms, introduces ferromagnetism at room temperature in II-IV-V$_2$ semiconductors. In addition, it has been found that rare-earth (RE) atoms can be incorporated into I-III-VI$_2$ materials and show photoluminescence in both visible and infrared spectral region. In this review, optical and magnetic properties of TA and RE in chalcopyrite type crystals are discussed.

KEY WORDS: Transition atoms, rare earth atoms, optical absorption, photoluminescence, electron spin resonance

1. Introduction

Ternary compounds of the I-III-VI$_2$ and II-IV-V$_2$ types, crystallizing in the tetragonal chalcopyrite structure, have been attracting much interest due to their promising photovoltaic, luminescent and nonlinear optical properties.[1]

Transition atom (TA) impurities have been known to introduce deep levels in the band gaps of semiconductors, which not only control a concentration and a type of conducting carriers but also act as activators or killers of luminescence.[2] The optical absorption and luminescence properties of ternary compounds depend not only on the charged state of TA impurities but also on the site, which the transition atom occupies. Therefore, the charged state can be determined from optical measurements.

It has been known from emission spectroscopy, that contamination of I-III-VI$_2$-type compounds occurs dominantly by Fe and Cr,[3] whereas ESR results indicate that the main contaminants are Fe and Ni, the valence state and the relative amount of these elements in each valence state being dependent on stoichiometry.[4]

We have tried to determine the type and valence states of TA impurities in the crystals of CuAlS$_2$ grown by the chemical vapor transport technique (CVT) using iodine as a transporting agent by 1) changing the position of the Fermi level in the band gap by stoichiometry-alternation caused by thermal treatments under different atmospheres or by doping with donor or acceptor-like impurities and by 2) controlling the resultant change in optical and ESR spectra. We have also studied single crystals of CuInSe$_2$ prepared by normal freezing method and CuGaSe$_2$ grown by traveling heater method (THM).

While Fe and Cr ions have been studied in unintentionally-doped CuAlS$_2$ host as residual impurities, all the other TA ions of the iron group, i.e., Ti, V, Mn, Co and Ni have been introduced into the host semiconductor by intentional doping and then investigated by optical and ESR techniques.[5]

Chalcopyrite type I-III-VI$_2$ compounds are considered capable of containing transition elements, since the mineral CuFeS$_2$ contains Fe as its constituent element. CuFeS$_2$ is an antiferromagnetic material (Néel temperature T_N~850 K) whose reduced moment (3.85 μ_B per Fe) has been explained in terms of energy band scheme of this material. Heavily Fe-doped crystals, or CuAl$_{1-x}$Fe$_x$S$_2$ alloys are therefore investigated to understand the change of Fe 3d-electronic states from its localized scheme to band scheme.[6]

We have also been investigating optical and ESR spectra of 4d-transition atoms in chalcopyrite materials. As a first example we studied Mo-doped CuAlS$_2$ single crystals.[7] A motivation of this study comes from solar cells research, in which Mo is employed as a back electrode for a CuInGaSe$_2$ solar cell-structure and possibility of incorporation of Mo into the active layer is suspected.

In recent years, III-V compounds doped with transition atoms are attracting interest as magnetic semiconductors for next-generation spin-electronics device applications. However, despite many efforts made by a number of researchers, the highest Curie temperature reported to date was 110 K in GaMnAs, which is far below the room temperature. The authors reported that CdGeP$_2$ doped with Mn exhibits ferromagnetism at room temperature,[8] the discovery having shown potentiality of II-IV-V$_2$ compounds as novel host materials for magnetic semiconductors.

Incorporation of rare-earth ions in chalcopyrite lattice has also been studied.[9, 10, 11] Luminescent properties have been systematically studied in a series of rare-earths in CuAlS$_2$. It has been found that light rare-earth elements can be incorporated into the chalcopyrite lattice leading to characteristic luminescence of these elements. Enhancement of emission efficiency by simultaneous doping of other impurity species has also been discovered.

Transition elements and rare earths seem to be more easily incorporated into the chalcopyrite lattice than into other binary compound semiconductors. This is partly due to the flexibility in structure and valence of this material, caused by the fact that two different cation sites exist in this crystal.

In this review, optical and magnetic studies of TAs and REs in chalcopyrite type semiconductors are summarized.

2. General Approach to the TA Impurities in Ternaries

Being brought into the chalcopyrite crystal lattice, the TA ion will experience the tetragonal crystal field of its four anion-ligands. Thus the symmetry will be lowered to D$_{2d}$, and the energy levels of the ion can be obtained as eigenvalues of a Hamiltonian

$$H = H_{\text{o}} + H_{\text{cr}}(\text{T}_{\text{d}}) + H_{\text{cr}}(\text{D}_{2d}) + H_{\text{LS}} , \quad (1)$$

where H_{o} is the free ion Hamiltonian, including kinetic energy of electrons in the d-shell and the potential energy of the electron-electron and electron-nucleus interaction, $H_{\text{cr}}(\text{T}_{\text{d}})$ and $H_{\text{cr}}(\text{D}_{2d})$ represent the energy of the cubic and tetragonal components of the crystal field, respectively, and H_{LS} is the energy of the spin-orbit interaction.

The free ion Hamiltonian H_o includes the term, representing the Coulomb repulsion of electrons, which is characterized by the Racah parameters B and C, which, in their turn, are the combinations of Slater's integrals involving radial parts of one-electron functions. The cubic crystal field is described by the parameter Dq, where D is the potential constant and q is the so-called radial integral, inducing the splitting of the free ion originated terms due to the effect of the crystal field.

The spin-orbit perturbation operator H_{LS} in a many-electron system comprise the scalar product of the total angular momentum L and the total spin S, i.e. $H_{LS} = \lambda L S$, where λ is the spin-orbit coupling parameter.

For the ions with 3d electronic configuration we have

$$H_o\ (\approx 10^4\ cm^{-1}) > H_{cr}(T_d) > H_{LS}(\approx 10^2\ cm^{-1})\ ,\quad (2)$$

or the so-called *intermediate crystal field* situation. This means that the multiplet splitting is greater than the cubic crystal field splitting, and this is greater than the spin-orbit splitting. Consequently, these effects are usually considered in that order.

In the intermediate crystal-field approximation the ligand field is treated as interacting only with the orbital momentum L, the effect of the ligand-field being to lift the $(2L+1)$ degeneracy of the free ion terms, while interaction with the spin states occurs through the mechanism of the spin-orbit coupling.

Another effect of the intermediate crystal field on the ion of the 3d-group is that, as the ion is being immersed into the ligand-field, its total angular momentum L loses the ability of free rotation to the effect that L will be partially or totally quenched. As a result the ions of the 3d-group usually exhibit g-values close to that of an electron spin (g_o=2.0023), the experimentally observed deviations of the g-values from g_0 being caused by the non-vanishing contributions from L for the orbital triplets, as well as by mixing of states of different orbital degeneracy via the spin-orbit coupling, the latter effect being expressed as $g-g_o = 8/10Dq$.

On the other hand, for the ions with 4f electronic configuration the interaction of 4f-shell electrons with the ligand field is smaller than the spin-orbit coupling, since the electrons of the 4f-shell are to the large extend not "valence" electrons but "inner" ones, which is due to the screening of the 4f-shell by the diffuse outer electron shells 6s and 5p. In this case

$$H_o > H_{LS} > H_{cr}(T_d) > H_{cr}(D_{2d})\qquad (3)\ ,$$

and we have the "weak crystal field" situation. The behavior of 4f electrons in the ligand field in this case is treated in terms of the resultant momentum J, in the first approximation the effect of the crystal field being partly to raise the $(2J+1)$ degeneracy of each level of the spin-orbit multiplet of given J. Contrary to the 3d-group ions, in the ions of the 4f-group quenching of the orbital momentum by the crystal field is only a minor effect, so the ground states carry large amounts of both orbital and spin momentum, giving rise to experimentally observed abnormally large g-values.

The above described simple crystal-field theory approach is based on the assumption of pure electrostatic forces, i.e. polar bonds. For the ions with 3d electronic configuration we expect, however, the considerable overlap of the 3d-shell-originated orbitals of the TA ion with those of the nearest neighbors. This effect of covalency is treated by the molecular orbitals theory,

which predicts a decrease in the values of the parameters B, C and, to the contrary, an increase in Dq with increasing covalency of bonding. Owing to the uncertainties in the values of Dq, B, C and all these parameters are usually treated as adjustable ones, which are chosen as to fit the energy differences, observed in the experimental optical spectra.

The overlap of TA ion orbitals with those of the ligands may also lead, under optical excitation, to the electronic transitions from the ion to the ligand or vice versa, or the so-called charge-transfer transitions, the intensities of these transitions being of two or three orders of magnitude higher than those for the d-d transitions.[12] The charge transfer transitions, which can also be considered as a photoionization of deep TA impurities, have been found to take place in various ternaries and are usually observed as strong absorption bands or as a photoionization threshold in the absorption spectra.[2]

The charge transfer transitions in ternaries are believed to occur from the valence band of the host compound to the 3d-shell originated orbitals of the TA ion (acceptor-like photo-excitation).[13] The reason for such an interpretation is that the molecular orbitals corresponding to the uppermost valence band states in ternary compounds are composed of sulfur 3p and Cu 3d orbitals, which makes possible the charge transfer from the ligand orbitals of the valence band to the 3d-shell originated orbitals of TA ion. On the other hand, the molecular orbitals of conduction band for ternaries are composed of 3s orbitals of monovalent and trivalent cations, which makes donor-like transitions from the 3d-shell to the conduction band parity forbidden.

3. Experiments

Single crystals of the ternary compounds were grown by the chemical vapor transport (CVT) technique in a closed system using iodine as a transporting agent. The powders of the corresponding compound, obtained by the direct melting (at temperature of 1300°C) of the constituent elements in a BN crucible held in a sealed quartz ampoule, were used as source materials for CVT. The ampoule was placed in a two-zone furnace to grow single crystals, the growth-zone temperature being 700°C and the source-zone temperature having been raised from 600°C to 850°C during 10 days.[14] Crystals were also obtained by the normal freezing method in the case of $CuInSe_2$,[15] and by the traveling heater method (THM) for $CuGaSe_2$.[16]

Doping of TA and RE in I-III-VI$_2$ crystals was done by addition of appropriate amount of elements to the starting materials for CVT.

Thermal annealing of the as-grown crystals in vacuum, chalcogen vapor and in the presence of Cu were carried out for 50 hr at 650°C. The obtained samples were characterized by the thermal probe and four-probe methods to determine their resistivities and conductivity type, respectively, as well as by the electron probe microanalysis (EPMA) to determine their composition.

ESR spectra were taken at 4.2 - 300 K with a JEOL JES-RE2X X-band spectrometer with the microwave power of 5 mW. Light-induced ESR spectra were also measured using white light of a 150-W Xe lamp monochromated by a Ritsu MC-10 grating monochromator, the spectral resolution being about 1 nm.

Optical absorption measurements were carried out at room temperature (RT) by using a BOMEM Type MB100 Fourier Transform IR spectrometer for middle-IR region and a HITACHI Type U-3410 Spectrophotometer for near-IR to near-UV wavelengths (300-2400 nm).

Photoluminescence (PL) spectra were measured between 20 K and room temperature (RT) using different excitation sources; the 365-nm line of a 150 W super-high pressure Hg-lamp, the 325-nm line of a Kimmon Electric CD3101R-1M He-Cd laser (10 mW), and the 514 nm line of Ar^+ ion laser (100 mW). The emitted light was dispersed by a JASCO CT-50C monochromator (focal length of 50 cm) with a 1200 groove/mm-grating blazed at 500 nm, and detected by a Hamamatsu R928 photomultipler. The photoluminescence excitation (PLE) spectra were measured using a 150-W Xe-lamp combined with a Ritsu MC-10N monochromator as an excitation source and using a JASCO CT-25C monochromator (focal length of 25 cm) combined with the R928 photomultiplier for detection of the emission. For IR emission, the emission was excited by the 514.5-nm line of an argon-ion laser, dispersed by a JASCO CT-25C monochromator, and detected by a liquid-nitrogen-cooled Ge detector (Northcoast EO-817L) and amplified by a lock-in amplifier.

Magneto-optical Kerr spectra were measured by using polarization modulation technique with a photoelastic modulator in the photon energies ranging between 1.2 and 5 eV at room temperature.[17] The maximum applied magnetic field was 1.7 T.

4. Optical and ESR studies of 3d-transition elements in chalcopyrite semiconductors

4.1 Undoped crystals of $CuAlS_2$

$CuAlS_2$ is the widest band-gap member of the ternaries, which has been found to emit strong green and blue photoluminescence (PL) and, therefore, is considered to be one of perspective materials for blue and green light emitting device realization.[18] Bulk single crystals of $CuAlS_2$ usually exhibit p-type conductivity with resistivity higher than 10^4 ohm-cm and hole mobility lower than 3 cm^2/Vs.[19] The high resistivity values
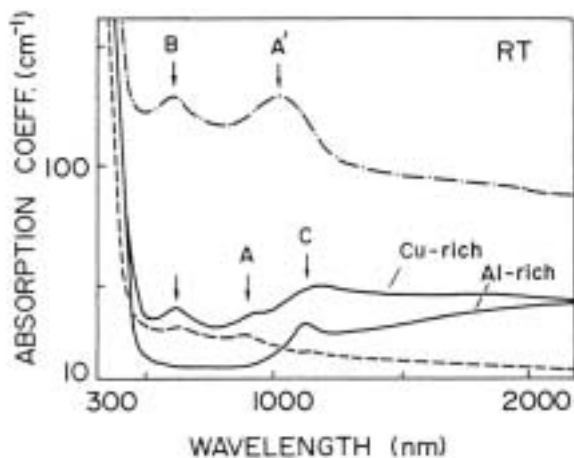

Fig. 1 Optical absorption spectra of the stoichiometric undoped $CuAlS_2$ (dashed curve), Cu- and Al-rich undoped $CuAlS_2$ (solid curves), as well as of the crystals obtained from the starting elements, including Fe and Cr impurities in the concentration of 20 ppm and 50 ppm, respectively (dot-dashed curve) [29]

imply that materials under consideration are highly compensated ones and the Fermi level position is located close to the center of the band gap. A defect whose energy level is located close to the center of the band gap will gain or lose electrons as the Fermi level passes through the demarcation level of different charged states associated with this defect. The position of the Fermi level in the band gap can be influenced by appropriate thermal treatments of the crystal or even by application of voltage in some junction devices. If any of the charged states of the defect are paramagnetic (with unpaired spins), then electron spin resonance (ESR) technique can be applied to monitor the motion of the Fermi level near the demarcation level of the defect.

The typical absorption spectra of undoped $CuAlS_2$ crystals, obtained from high-purity elements with the specified concentrations of Fe, Cr and Ni being less than 5 ppm, 2 ppm and 1 ppm, respectively, are shown by a dashed curve in Fig. 1. The spectrum of undoped nominally stoichiometric $CuAlS_2$ consists of two broad bands A and B at 920 and 620 nm, respectively, originated from charge-transfer transitions related to residual Fe^{3+} ions, substituting for Al sites.[20] Most of the crystals also exhibit a broad absorption C-band peaked at 1150 nm, as well as a broad weak absorption at 1900 nm, the spectral position of the latter band being approximately the same as was observed in Cr-doped CdS.[21] We attributed the band at 1900 nm to the intrasystem transitions $^5T_2$- ^5E in the 3d-shell-originated orbitals of Cr^{2+} ion. As the energy difference for this transition in Cr^{2+} ($3d^4$ electronic configuration) represents $10Dq$ plus the ground term stabilization energy due to the spin-orbit coupling, we estimated the value of Dq for Cr^{2+} in the $CuAlS_2$ host to be 540 cm^{-1}. Taking into account the strength of the C-band this band has been assigned to the Cr^{2+}-Cr^+ charge transfer transition.

The spectra of Cu-rich (nominal composition $Cu_{1.03}Al_{0.97}S_2$) undoped crystals exhibit the slight increase in intensities of A- and B-bands, whereas in Al-rich samples (composition $Cu_{0.97}Al_{1.03}S_2$) these Fe^{3+}-related bands are diminished or eliminated, the last result being in accordance with that obtained by Donohue et al.[3] These results can be explained taking into account that a large concentration of the defects of antisite disorder should be expected in Cu-rich and Al-rich crystals, these defects being the acceptor-like Cu_{Al}-defects for Cu-rich samples and the donor-like Al_{Cu}-defects for Al-rich samples.

These defects will influence the position of the Fermi level in the band gap of the host crystal, resulting in the change of valency of Fe ions, responsible for the A- and B-absorption bands. The effect of native defects formation on the absorption spectra will be discussed later.

The spectrum of the crystal, obtained from the starting elements, containing Fe and Cr impurities in high concentration (Fe 20 ppm, Cr 50 ppm), shows the great increase in absorption coefficient due to the strengthening of Fe and Cr-related absorption bands, the A-band in this case is shifted towards lower energies and labeled as A' (Fig. 1, dot-dashed curve).

The ESR spectra of undoped stoichiometric $CuAlS_2$ crystals at 110 K are shown in Fig. 2. The spectrum, taken under parallel orientation of the c-axis of the sample in relation to the external magnetic field H, consists of five fine structure transitions attributed to Fe^{3+} ions with $3d^5$ ($S=5/2$) electronic configuration.[22, 23]

In addition to the Fe-related transitions, a nearly isotropic line at $g = 11.95$ as well as an anisotropic line at $g = 8.15$ were found
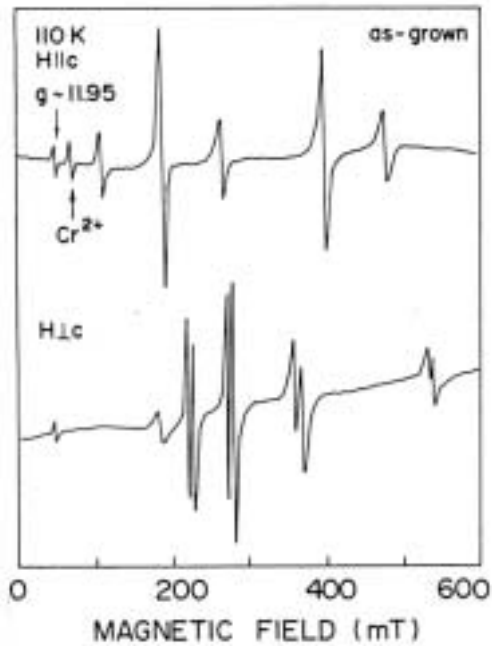
Fig. 2 ESR spectra of undoped nominally stoichiometric CuAlS$_2$ crystals for two different orientation of the magnetic field.[29]

to be present in undoped crystals. We cannot explain the nature of the line at $g = 11.95$ except that this line must be originating from some impurity or native defect, the ground state of which carries very large amount of orbital momentum. On the other hand, the anisotropic line at $g=8.15$ can be readily assigned to the transitions within the lowest orbital singlet ground state of Cr^{2+} ion on substitutional sites of tetragonal symmetry, since the anisotropic Cr^{2+}-related lines with g-values, close to the observed in this study, have been found in binary compounds CdS ($g = 7.75$)[24] and ZnSe ($g =7.837$).[25]

The spectrum of stoichiometric crystals, taken for orientation H⊥c, exhibits the same fine structure of Fe^{3+} ions as well as the unidentified line at $g =11.95$, the fine structure lines being split into two components due to the presence of two magnetically inequivalent metal sites in the chalcopyrite lattice. In this case the integral intensities of fine structure transitions approximately follow the theoretically predicted ratio 5:8:9:8:5, the most intense -1/2 ↔ +1/2 transition being in the center of the spectrum.

It should be noted in connection with Fe^{3+} impurity that, although the Fe^{3+}-originated fine structure in the ESR spectra, observed in this study, is similar to that observed previously in CuXS$_2$ compounds (X=Al, Ga, In),[22] the positions of all fine structure lines in our case are shifted towards lower values of the external magnetic field (i.e. to the higher g_{eff}-values) as compared with those previously reported.

If we take into account that not only of the valency of Fe ions, but also their positions in the lattice of the host crystal, depend greatly on the technology of the material preparation, then the shift of Fe^{3+}-originated fine structure can be explained under an assumption that Fe^{3+} ions in our crystals substitute for Al^{3+} sites, whereas in the crystals used in ref. 22, Fe^{3+} ions substitute for Cu$^+$ sites. The substitution of Al site by Fe causes greater lattice distortion around the resulting defect as compared with that in case of Cu-site substitution, since ionic radius of Fe^{3+} (0.63 Å) is larger than that of Al^{3+} ion (0.53 Å) but smaller as compared with Cu$^+$ (0.74 Å). Moreover, the second shell ligands surrounding of Fe$_{Al}$-defect is more covalent than that of Fe$_{Cu}$-defect since in the former case each of the four sulfur anions, surrounding iron impurity, forms bonds with two Cu cations (Cu-S bonds being highly covalent) and one Al cation (Al-S bonds being almost purely ionic), whereas in the latter case each S anion forms one bond with Cu and two bonds with Al.

The combined influence of the lattice strain and covalency can lower the symmetry around the substitutional defect, and results in the larger value of the cubic and axial components of the crystalline potential. We suppose, therefore, that Fe ions in our case substitute for Al sites, giving rise to the large crystal field splitting comparable with Zeeman splitting, caused by the external magnetic field. The same situation, i.e. Fe ions substituting for both cation sites, have been found to occur in CuGaS$_2$ compound containing iron as the residual impurity, where Fe have been found to form two types of substitutional defects - Fe$_{Cu}$ and Fe$_{Ga}$, the former being responsible for the infrared photoluminescence and the latter causing the green coloration of the crystals.[26]

The spectra of Cu-rich crystals were essentially the same as described above, whereas the spectra of Al-rich samples exhibit the decrease in the intensity of the Fe^{3+}- and Cr^{2+}-related ESR lines, which is in accordance with the results of optical absorption. In some Cu-rich samples as well as in all samples grown from contaminated starting elements, a broad line with g-values depending on orientation of the crystal and changing in the range of $g = 2.05$-2.31, has also been found, this line being attributed to the transitions within the lowest Kramers doublet of substitutional Ni$^+$ ion.[27] Moreover, the crystals, grown from the contaminated starting elements, have also exhibited well resolved 30-line ESR structure, attributed to Mn^{2+}configuration the sixfold spin degeneracy results in five fine-structure lines, each of which is split into six hyperfine lines by the nuclear spin I=5/2 of ^{55}Mn.[28]

4.2 Annealed crystals

The absorption spectra of S- and vacuum-annealed samples are shown in Fig. 3. It is seen from this figure that rising the pressure of S as well as the temperature of annealing results in the increase of intensity of the Fe^{3+}-related A- and B-bands, and
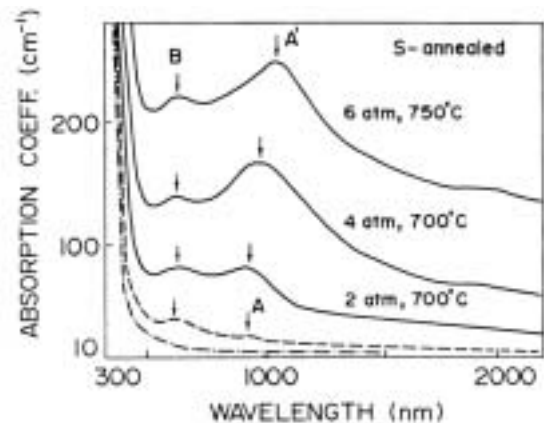

Fig. 3 Absorption spectra of S-annealed CuAlS$_2$ crystals (solid curves). The spectra of as-grown (dashed curve) and vacuum-annealed (dot-dashed curve) samples are also shown for comparison[29]

in the shift of the A band towards its spectral position in the Fe- and Cr-contaminated samples (Fig. 1, A'-band), as well as in the Cr-doped $CuAlS_2$ studied in ref. 2. Our Cr-doped samples have been found to exhibit the same shift of the A-band towards its position in the S-annealed samples. Therefore, the shifted A'-band is believed to be formed by both Fe- and Cr- related charge transfer transitions, the Fe-originated A-band and the Cr-originated C-band being superposed on each other and resulting in the A'-band. The Ni^{2+} impurity may also contribute to the strengthening of the A'-band since divalent Ni ions in $CuAlS_2$ host exhibit strong intra-system $^3T_1(F) - {}^3T_1(P)$ transitions, the spectral position of which correspond to that for the A'-band (see 4.3). ESR spectra of the crystals, annealed in S-vapor, show no remarkable changes as compared with the spectra of as-grown crystals, shown in Fig. 2.

Annealing of the crystals in vacuum for 60 h results in the decrease of intensity of A'- and B-bands, whereas vacuum annealing for 120 h completely eliminates this transitions (Fig. 3) and results in colorless crystals.

Vacuum and Cu-annealed crystal have been also found to exhibit drastic changes in their ESR spectra as shown in Fig. 4.[29] In this case the spectra at room temperature show only one isotropic line at $g_{//}=1.998\pm0.005$, that exhibits the fine structure, consisting of five components, which is shown in Fig. 4 for two orientations of the crystal. The structure observed has been assigned to the fine structure transitions of Cr^+ ion since 1) Cr^+ ion exhibit the isotropic g-value of 1.9995 in ZnS compound,[30] that is an isoelectronic analogue of $CuAlS_2$, and 2) the observed number of the components of fine structure agrees with the number of those that should be expected from the ion with $3d^5$-electronic configuration ($S=5/2$). The observed pattern is surely fine structure, not hyperfine one, because it is resolved up to the temperatures of 220 K, and because the components of the structure are not equidistant, which should have been expected for hyperfine interaction.

The observed changes in the ESR and optical absorption spectra of the $CuAlS_2$ crystals, caused by the thermal treatments in different atmospheres,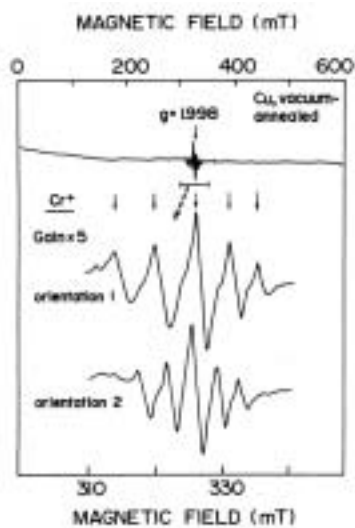 can be explained taking into account the energy level diagram of $CuAlS_2$ (Fig. 5), in which the energy levels, formed by donor-like and acceptor-like native and extrinsic defects, as well as the position of the Fermi level in relation to the positions of the Fe^{2+}/Fe^{3+} and Cr^+/Cr^{2+} demarcation levels, are shown.

Since as-grown $CuAlS_2$ crystals usually exhibit p-type conductivity with high resistivity values, we believe that in the as-grown crystals the Fermi level is shifted down a little from the midgap position, the Fermi level being lower than both Fe^{2+}/Fe^{3+} and Cr^+/Cr^{2+} demarcation levels. Therefore, in the as-grown crystals the Fe^{3+}- and Cr^{2+}-related signals should be observed in optical absorption and ESR spectra, which is in good agreement with the experimental results.

The thermal treatment in S-vapor will result in a decrease of concentration of sulfur vacancies V_S, and in the increase of concentration of cation vacancies V_{Cu} and V_{Al}. Since the former defects are donor-like and the latter defects are acceptor-like, the degree of compensation under S-annealing will be reduced, which was observed experimentally as an increase of conductivity of p-type samples. The reduction of the degree of compensation means that the Fermi level in the samples moves from its midgap position in highly compensated crystals towards the valence band, this movement resulting in the lowering of the Fermi level in relation to the demarcation levels of TA ions, i.e. Fe^{2+}/Fe^{3+} and Cr^+/Cr^{2+}, as compared with its position in as-grown samples. Therefore, both Fe and Cr ion impurities will be losing their electrons, this process resulting in the increase of concentration of Fe^{3+} and Cr^{2+} ions, which is observed as the increase of intensities of the absorption bands, originated from these ions, and in the decrease of concentration of Fe^{2+} and Cr^+ ions.

For vacuum-annealing the above described processes are reversed, the Fermi level moving up towards the conduction band due to the increase of concentration of Vs-defects, which results in the reduction of valency of Fe and Cr ions to their optically undetectable states Fe^{2+} and Cr^+.

The defects, responsible for the change of the degree of compensation of the $CuAlS_2$ under annealing and doping, the expected shift of the Fermi level, as well as the experimentally observed change in the optical absorption and ESR spectra of the crystals, are shown in Table 1.
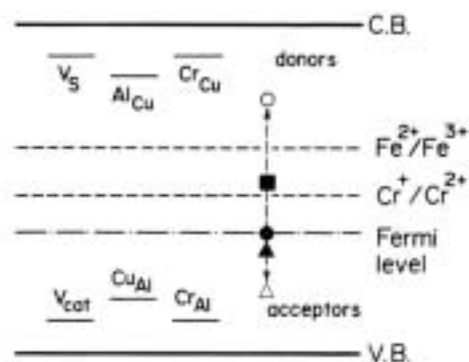
Fig. 4 ESR spectra of Cr^+ ion ($3d^5$ configuration) in Cu- and vacuum-annealed crystals of $CuAlS_2$.[29]

Fig. 5 A schematic energy level diagram of $CuAlS_2$: Fe, Cr.[29]

Table 1. The effect of the thermal treatments and doping on the optical and ESR spectra of CuAlS$_2$ crystals[29]

Treatments	Defects	Fermi level position	Observed changes in the spectra		
			Fe^{3+}	Cr^{2+}	Cr$^+$
As-grown :					
stoichiometric			+	+	0
Cu-rich	Cu$_{Al}$↑	↓	↑	↑	0
Al-rich	Al$_{Cu}$	↑	↓	↓	0
Cr-doped:					
Al-deficient	Cr$_{Al}$↑	↓	↑	↑	
Cu-deficient	Cr$_{Cu}$↑	↑	↓	+	↑
S-annealed	V$_S$↓,V$_{Cu}$↑	↓	↑	↑	
Cu-,vacuum-annealed	V$_S$↑	↑	0	0	↑

Table 2. Spectral positions of the absorption bands (center of gravity) for TA ions in CuAlS$_2$ host together with the list of parameters of TA ions in CuAlS$_2$ in comparison with those for ZnS (given in brackets)[5]

d^n.	Ions	Energy (cm^{-1})	Transition	Dq	B	λ	Ref.
d^2	V^{3+}	5700	$^3A_2\rightarrow{}^3T_2$	570	465	20	31)
		9090	$^3A_2\rightarrow{}^3T_1$	(560)	(465)	(40)	
		14900	$^3A_2\rightarrow{}^3T_1(P)$				
d^4	Cr^{2+}	5300	$^5T_2\rightarrow{}^5E$	540			
d^5	Mn^{2+}	17860	$^6A_1\rightarrow{}^4T_1$				
		19190	$^6A_1\rightarrow{}^4T_2$	580	335		32)
		20890	$^6A_1\rightarrow{}^4A_1+{}^4E$	(545)	(500)		33)
		22420	$^6A_1\rightarrow{}^4T_2$				
d^7	Co^{2+}	6990	$^4A_2\rightarrow{}^4T_1$	390	520	-185	34)
		13280	$^4A_2\rightarrow{}^4T_1(P)$	(375)	(610)	(-195)	35)
	Ni^{3+}	6670	$^4A_2\rightarrow{}^4T_1$	370			
d^8	Ni^{2+}	4530	$^3T_1\rightarrow{}^3T_2$	500	440	-220	36)
		10350	$^3T_1\rightarrow{}^3T_1(P)$	(475)	(560)	(-250)	35)
d^9	Ni$^+$	3566	$^2T_2\rightarrow{}^2E$	290		-410	
		3984					

Table 3. Spin-Hamiltonian parameters for TA ions in CuAlS$_2$ host with D and A values being given in units of 10^{-4} cm^{-1} and k being the co-valency reduction factor[5]

Conf.	Ion	$g_{//}$	$g_\perp$	D	$A_{//}$	$A_\perp$	K	Ref.
d^1	Ti^{3+}	1.902	1.978		26.3	8.3	0.81	39,40)
d^2	V^{3+}	1.973		1900	65.0			39)
d^5	Fe^{3+}	2.020		900				23)
d^6	Fe^{2+}	2.187	2.037	11900			0.8	37)
d^7	Co^{2+}	2.138	2.030	10000	20.6	11.3	0.68	38)
d^9	Ni$^+$	2.051	2.330		13.0	61.0	0.68	36,27)

4.3 TA-doped crystals

We have carried out doping of the CuAlS$_2$ compound with TA impurities such as Ti, V, Co and Ni by adding these elements into the starting mixture of the constituent elements used for synthesis of the compound,[14] whereas doping with Fe and Mn has been performed during the crystal growth.

In Fig. 6 we have summarized the optical absorption spectra of the CuAlS$_2$ crystals doped with TA impurities.[5] The parameters of the TA ions in CuAlS$_2$, such as the cubic crystal field parameter Dq, Racah parameter B and the spin-orbit coupling parameter, deduced from the absorption spectra, are listed in Table 2, whereas Table 3 summarizes the spin-Hamiltonian pa-
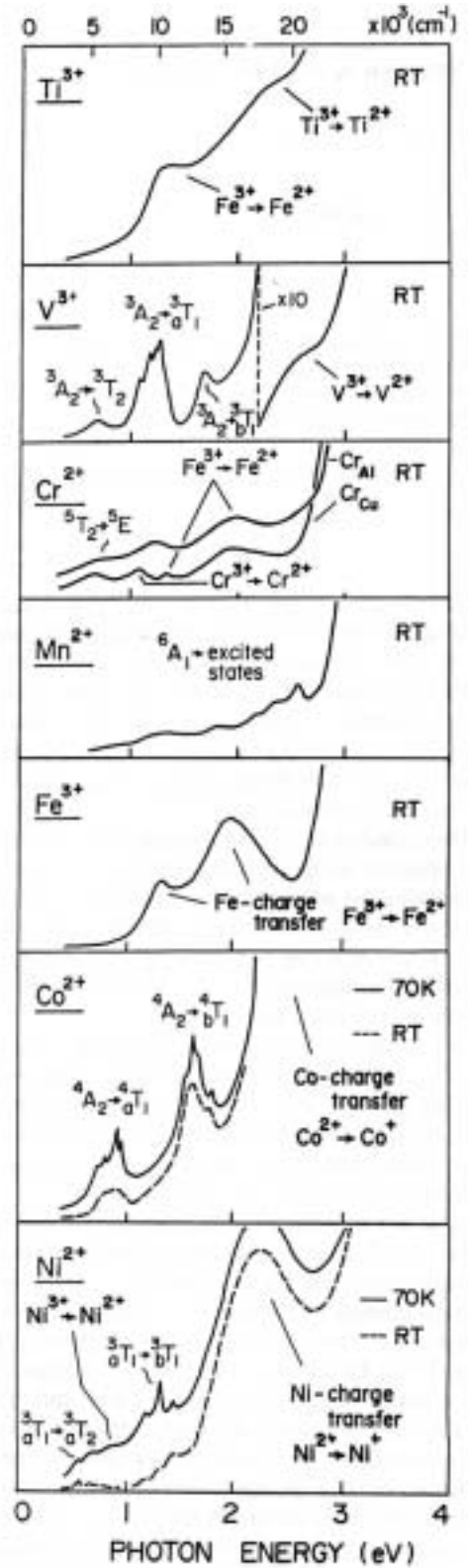

Fig. 6. Compilation of observed optical absorption spectra of TA impurities in CuAlS$_2$.[5]

rameters, derived from ESR spectra, these parameters being g-values for two principal orientations of the c-axis of the crystal in relation to the external magnetic field, the non-cubic crystal field parameter D, the electron spin - nuclear spin interaction parameters $A_{//}$ and $A_\perp$, and the covalency reduction factor k.

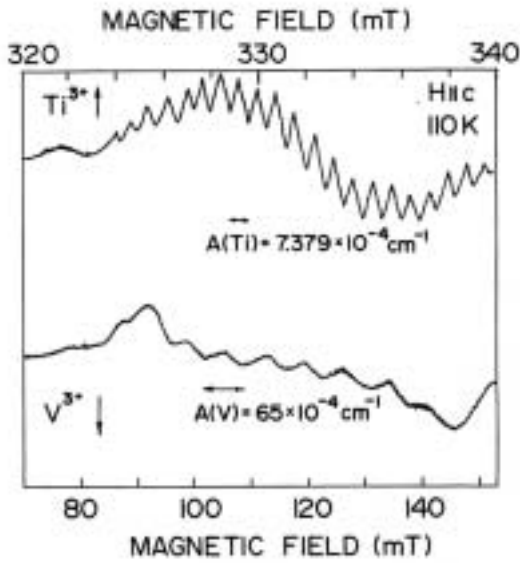Let us consider the TA impurities one by one in the order of filling of their 3d-shell.

Fig. 7. Hyperfine structure of Ti^{3+} and V^{3+} ions in $CuAlS_2$.[39]

4.3.1 Titanium (d^1)

Titanium ion has been found to be present in the $CuAlS_2$ host in its trivalent form, having d^1 electronic configuration.[39, 40] Absorption spectra exhibit only the charge transfer band at 19200 cm^{-1} superposed on a steeply rising band edge absorption of the host crystal. The ESR spectrum of the Ti-doped $CuAlS_2$ exhibits one intense line due to the transitions within the lowest Kramers doublet ^2B split from the state of ^2E symmetry by the tetragonal component of the crystal field. At low temperatures the Ti^{3+}-originated ESR signal exhibits two types of hyperfine (HF) structures: a HF splitting arising from nuclei of ^{47}Ti and ^{49}Ti having the nuclear spin 5/2 and 7/2, respectively, as well as a ligand HF splitting into 21 well resolved, equidistant components due to the interaction with four ^{27}Al nuclei in the second shell surrounding of the substitutional Ti ion, the latter being shown in the upper figure of Fig. 7. Taking into account the value of the nuclear spin I=5/2 for ^{27}Al, the observed number of
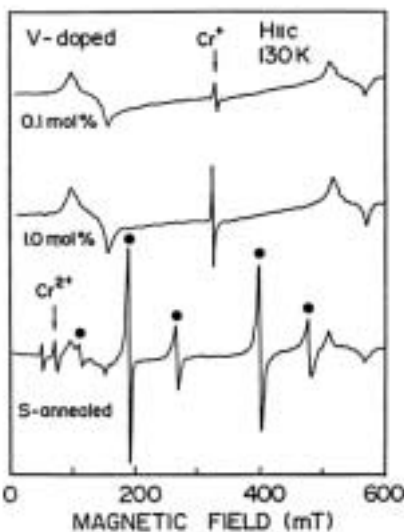
Fig. 8. ESR spectra of V-doped $CuAlS_2$. The lines marked by dots show the Fe^{3+}-related fine structure.[39]

HF structure components allows unambiguous identification of Ti being substituting for Al sites in $CuAlS_2$.

On the basis of the spin-Hamiltonian parameters for Ti^{3+} ion, derived from the ESR data in ref. 38, the optical transitions from the ground state $^2B(E)$ to excited states of $^2E(T_2)$ and $^2B(T_2)$ symmetry have been predicted to occur at 9540 and 10030 cm^{-1}. These transitions, however, have not been detected so far.

4.3.2 Vanadium (d^2)

Vanadium is also trivalent in $CuAlS_2$ and exhibits three absorption bands originated from intrasystem (the same spin multiplicity) crystal field transitions from the ground state $^3A_2$ to the excited states of ^3T_i (i=1,2) symmetry, [14] with the values of Dq and B being shown in Table 2 in comparison with these values for V^{3+} in ZnS. [31]

Figure 8 shows the ESR spectra of V-doped, as well as subsequently S-annealed $CuAlS_2$ crystals. The ESR spectra exhibit two broad fine structure lines, this result being similar to that for V-doped CdS.[41] The observed fine structure has been assigned to the transitions within the ground orbital singlet (spin triplet) state split by the effect of the tetragonal component of the crystal field combined with the spin-orbit interaction into spin doublet and spin singlet states, with the splitting between them (D=0.19 cm^{-1}) being smaller than the energy of the microwave quantum $\hbar\omega$.

At temperature below 120 K each of the fine structure lines exhibits splitting into eight HF components due to the HF interaction with ^{51}V nuclei (I=7/2), as shown in the lower curve in Fig. 7, the value of the HF splitting parameter A (Table 3) being in good agreement with that for V^{3+} in ZnS. The annealing experiments suggest that vanadium in $CuAlS_2$ substitutes for Cu sites. [29]

4.3.3 Chromium (d^4 & d^5)

Chromium supposedly substitutes for both Cu and Al sites in $CuAlS_2$, divalent chromium having been detected in both absorption and ESR spectra, which was discussed in 4.2. [3] In a tetrahedral crystal field, the ground ^5D term of a free Cr^{2+} ion is split into a triplet $^5T_2$ and doublet ^5E, with the former being lowest. The threefold orbital degeneracy of the $^5T_2$ state is lifted by the tetragonal crystal field, the triplet being split into a singlet and a ground doublet, upon which the spin-orbit interaction acts. The energy spectrum of the resulting lowest non-Kramers doublet in a magnetic field has been described for CdS host by the spin-Hamiltonian given in ref. 24 with an effective spin of S'=1/2, which differs from its value S=2 for the free ion. The resonant absorption within the lowest doublet, split by the spin-orbit interaction, is allowed only when a microwave-frequency magnetic field is directed along the c-axis.

The resultant g-value for Cr^{2+} in $CuAlS_2$ is highly anisotropic, with g_{eff} = 8.15 and g_{eff} ~0. The splitting energy between the two lowest singlets, causing the ESR, has not been determined so far due to theoretical difficulties, involving those of necessity to treat this problem in terms of a Jahn-Teller distortion of Cr^{2+}-related states by random vibration modes.

Monovalent chromium with a $3d^5$ electronic configuration has been detected in the $CuAlS_2$ host as the fine-structure ESR-line consisting of five components (Fig. 4), originating from the transitions between the three spin doublet states, split from the $^6S_{5/2}$ free-ion ground state by the effect of the crystal field and spin-orbit interaction.

4.3.4 Manganese (d^5)

Manganese in $CuAlS_2$ is believed to substitute for Cu sites and exhibits several weak crystal field transitions associated with Mn^{2+} center (Fig. 6), the observed transitions, as well as the crystal field and Racah parameters for the Mn^{2+} ion being shown in Table 2, [32] in comparison with those for ZnS:Mn [33]

A strong red photoluminescence band peaked at 1.96 eV has also been observed in Mn-doped $CuAlS_2$, whose excitation spectrum is in agreement with the absorption spectrum. [32] Time-resolved PL spectra are shown in Fig. 9, in which it is found that the spectrum shows a DA-pair band at 3 eV immediately after excitation, which looses its intensity with the time evolution to give up its intensity to the Mn^{2+}-related ligand-field luminescence. [42]
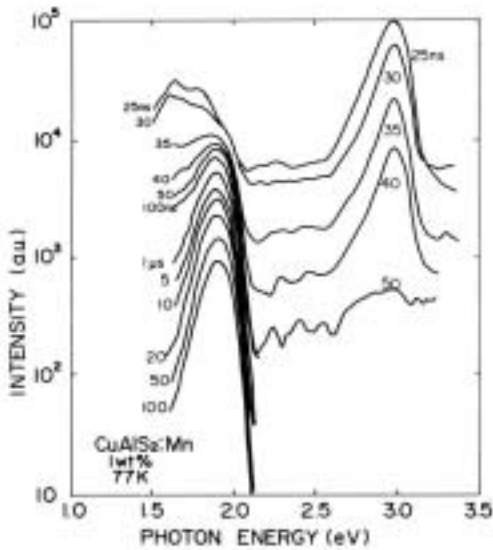
Fig. 9 Time-resolved photoluminescence spectrum in a 1% Mn-doped $CuAlS_2$ single crystal measured at 77 K. [42]

The Mn-doped $CuAlS_2$ has been known to show electroluminescence spectrum similar to the photoluminescence spectrum [32, 43] The DC-EL device with Al-CuAlS$_2$:Mn-Al diode structure was fabricated and its EL characteristics were reported. [44]

The ESR spectrum of $CuAlS_2$ exhibits the well-resolved 30-line structure, originated from the transitions between energy levels, split from the six-fold spin-degenerate ground state of Mn^{2+} by the effect of the crystal field and spin-orbit interaction (five lines of the fine structure) combined with the effect of electron spin - nuclear spin interaction (each of the fine structure lines splits into six HF components since $I(^{55}Mn) = 5/2$). The similar ESR spectrum has been observed for Mn^{2+} in $CuGaS_2$, in which case, however, Mn is believed to substitute for both cation sites. [28]

4.3.5 Iron (d^5 & d^6)

Iron is the most extensively studied TA ion in ternaries, including the $CuAlS_2$ compound. The trivalent iron introduces two charge transfer transitions, [20] causing the green coloration of the crystals, and is supposed to substitute for both Cu and Al sites, giving rise to two different types of the ESR spectra (see 4.1), with the values of g-factor and D for Fe^{3+} substituting for Cu-sites being listed in Table 3

The ESR spectrum of divalent iron in $CuAlS_2$ has been observed at 20 K, [27] and found to consist of a single line with $g_{eff} \sim 9.5$ and $g_{eff} \sim 0$. The Fe^{2+}-related ESR signal has been interpreted as arising from the transitions within the lowest spin doublet of Ms = 2 split from the ground state of ^5B symmetry by the spin-orbit interaction, the ^5B state, in its turn, having been split from the ^5D free ion ground term by the effect of the crystal field. The ESR results were analyzed with the spin-Hamiltonian given in ref. 35 for $S=2$ in tetragonal symmetry, the analysis yielding the g and D values, shown in Table 3.

Most of the as-grown crystals prepared by CVT method exhibit a broad absorption band that covers from near-IR to visible region, which has been attributed to the charge-transfer transitions relating to Fe^{3+} ions substituting group III elements, as have been shown in our previous report, whereas the IR absorption spectra for $h\nu < 6000 cm^{-1}$ have been found to exhibit no remarkable features in all the investigated compounds. A sharp photoluminescence peak at 5804 cm^{-1} due to the $^4T_1 - ^6A_1$ crystal field transitions in the Fe^{3+} ion has also been observed in $CuAlS_2$. [45] A sharp IR photoluminescence line spectrum has been also observed in as-grown crystals of $CuAl_{1-x}Ga_xS_2$ system as shown in Fig. 10 and attributed to transitions from $^4T_1 \Rightarrow ^6A_1$ in Fe^{3+} occupying the Cu-site. [46]

Annealing of the crystals in vacuum, however, results in a reduction of the intensities of the charge-transfer band (related to Fe on group III) in near-IR to visible region and a simultaneous appearance of broad IR bands in $CuInSe_2$, $CuInS_2$, and $CuGaS_2$ crystals as shown in Fig. 11. [47] The absorption is peaked at about 3300 cm^{-1} in $CuInSe_2$, 4000 cm^{-1} in $CuGaS_2$, and is split into two partially resolved subbands peaked at 3200 cm^{-1} and 3900 cm^{-1} in $CuInS_2$, and similar subbands at 3400 cm^{-1} and 4400 cm^{-1} in the case of $CuAlS_2$. The absorption bands, shown in Fig. 11, have been attributed to the Fe^{2+} impurity occupying
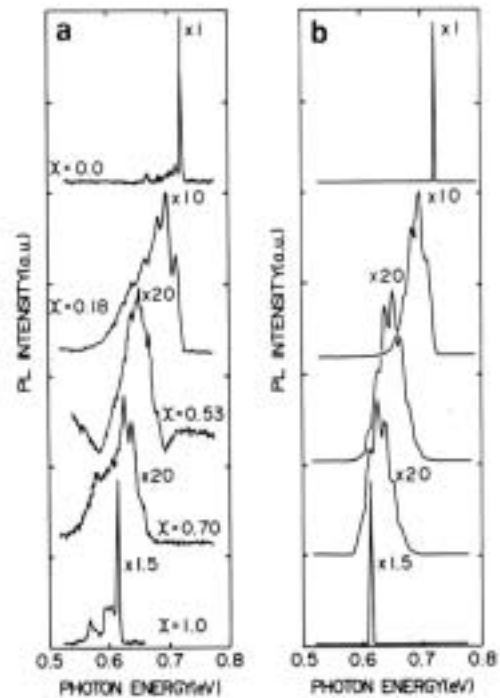

Fig. 10 (a) Photoluminescence spectra associated with the ligand-field transition $^4T_1 \rightarrow ^6A_1$ of 3d^5 manifold in as Fe^{3+} ion in single crystals of $CuAl_{1-x}Ga_xS_2$ system. (b) Simulated spectra assuming nine equally spaced Gaussian lines with intensities given by binomial distribution. [46]
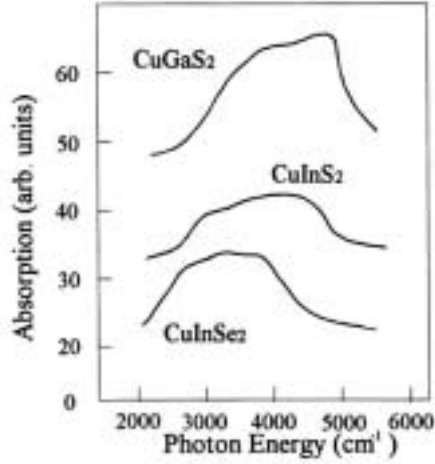
Fig.11. IR absorption spectra in vacuum-annealed $CuGaS_2$, $CuInS_2$ and $CuInSe_2$ crystals grown by CVT.[47]

Fig.12. Type-1 ESR spectrum in as-grown IT-CuGaSe$_2$ single crystal.[49]

Fig. 13. Type-2 ESR spectrum of a CVT CuGaSe$_2$ single crystal[49]

Fig.14 Angular dependence of C line in CVT CuGaSe$_2$.[49]

group-III-sites in the crystal lattice of the ternaries. This assumption is supported by the results of the previous studies of the binary semiconductors, where the Fe^{2+} ion has been found to exhibit a broad absorption center, for example, at about 3400 cm^{-1} for ZnS.[48] Taking into account also the ESR results, which will be discussed below, we attribute the IR absorption bands to the intrasystem optical transitions $^5E \Rightarrow {}^5T_2$ in the Fe^{2+} ion having $3d^6$ electronic configuration.

CuGaSe$_2$ single crystals grown by the CVT technique show two types of ESR spectra associated with the Fe impurity; Type-1 and Type-2.[49] The Type-1 spectrum is plotted in Fig.12. The crystal was rotated around the <110> axis. In this spectrum several anisotropic lines denoted as **B** were found at 110-130 mT, 400-430 mT and 900-950 mT. The spectral feature is similar to that of Fe^{3+} in CuInSe$_2$, and suggests that Fe-X complex is involved.[49] The Type-2 spectrum shown in Fig.13 was observed in some of the IT crystals.[50] In this spectrum, in addition to the resonance line **I** attributed to Se vacancy,[51] ESR lines marked as **C** was observed, whose resonance field varied strongly with the angle θ between the direction of magnetic field and the crystal axis. The angular-dependence of Fe^{2+} signal was theoretically analyzed and found to obey a $1/\cos\theta$ relation. The signal-**C** is plotted by closed circles in Fig. 14 as a function of the angle θ. The straight curves in the figure are $1/\cos\theta$ functions that provide the best fit to the experimental points. A fourfold symmetry is clearly observed. Since no fourfold symmetry exists in the chalcopyrite lattice, this angular dependence suggests an existence of two Fe sites with mutually perpendicular twofold axes.

Our recent IR absorption study clearly showed an existence of an absorption peak around 3200 cm^{-1} that can be assigned to the ligand-field transition in Fe^{2+}. Therefore, we believe that our C-signal is due to the Fe^{2+}.

Annealing in Se atmosphere completely quenched the signal **C** and the signal **I,** and introduced the type-1 spectrum with B signal relating to Fe^{3+}. Quenching of the signal **I** suggests disappearance of the V_{Se} donor, which in turn may introduce a downward shift of the Fermi level E_F below the demarcation level delineating Fe^{2+} and Fe^{3+} valence states. This is consistent with our experimental finding that the Fe^{2+}-signal disappeared and Fe^{3+}-related signal appeared by Se-annealing.
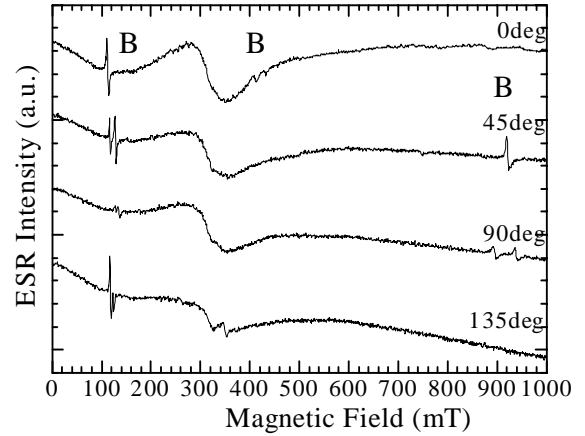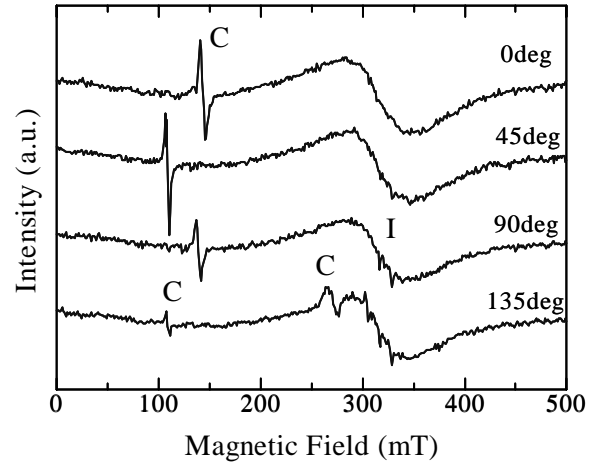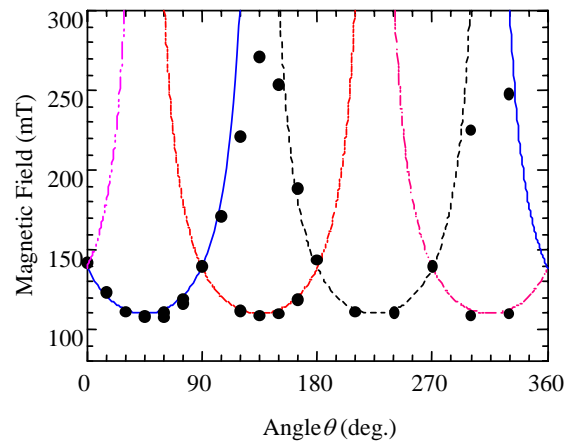
4.3.6 Cobalt (d^7)

Cobalt in CuAlS$_2$ is also divalent and exhibits two strong absorption bands resulting from the ligand-field transitions,[34] the deduced values of the parameters Dq, B and λ being shown in Table 2 together with those for Co^{2+} in ZnS,[35] as well as a very strong charge transfer transition causing the large observed red shift of the absorption edge of the host crystal down to 2.2 eV (Fig. 6).

The ESR spectrum of Co^{2+} in $CuAlS_2$ shows only one transition within the lowest 1/2 Kramers doublet, which indicates that the non-cubic crystal field splitting D is considerably larger than the microwave quantum $\hbar\omega$ (Table 3). [38] The above transition is split into eight hyperfine components due to the interaction with ^{59}Co nucleus having $I = 7/2$. The question, of which cation site the Co^{2+} ion substitutes, remains unsolved.

4.3.7 Nickel (d^7, d^8 & d^9)

Trivalent nickel is supposed to exhibit the broad absorption band peaked at 6670 cm^{-1} (Fig. 6). Divalent nickel exhibits two crystal field transitions, as well as a strong charge transfer band peaked at 18200 cm^{-1} (2.25 eV), caused by Ni^{2+}-Ni^+ photoionization transitions (Fig. 6). Ni^{2+} shows no ESR signal, which can be explained taking into account that 1) Ni^{2+} is a non-Kramers ion and 2) the ground state of the Ni^{2+} ion in $CuAlS_2$, which results from the crystal field and spin-orbit splitting of the free ion ^3F ground term, is the singlet state of A_1 symmetry, which can not be split even by the non-cubic component of the crystal field.

The ESR spectra of the $CuAlS_2$ crystals, annealed in various atmospheres are shown in Fig. 15. The observed ESR signals have been interpreted as follows:

—a signal of Fe^{3+}, consisting of five fine structure transitions, [29] which are split into two components for perpendicular orientation of a magnetic field in relation to the c-axis of the crystals (Fig. 15(e)) due to the presence of two magnetically inequivalent metal sites in the chalcopyrite lattice, [22]

—a highly anisotropic signal with $g_{//}$~8.5, $g_\perp$→0, originating from transitions within the lowest non-Kramers doublet of Cr^{2+} ion, [29]

—an anisotropic signal with $g_\perp$~$2g_{//}$~4.38, which has been tentatively attributed to transitions within the ±1/2 Kramers doublet of Ni^{3+}, this assignment being based on the similar results for Ni^{3+} in the $CuGaS_2$ compound, [52]

—a superposition of two ESR signal, i.e., a signal of Cr^+, consisting of five fine structure lines with isotropic g=1.998, [29] and that of Ni^+, exhibiting one slightly anisotropic transition ($g_{//}$=2.05, $g_\perp$=2.31) within the lowest Kramers doublet, the observed anisotropy of the Ni^+ signal being caused by the spin-orbit mixing of the lowest doublet with the upper Kramers doublets, [27] and

—a nearly isotropic signal at g~11.95, originating from some unidentified impurity, the ground state of which carries a large amount of orbital momentum. [29]

4.3.8 Summary of 3d-TA ions

To end up with TA ions of the iron group three more points should be noted, i.e.

1) All TA-doped $CuAlS_2$ crystals exhibit an apparent red shift of the absorption edge from its value of 3.3 eV for undoped crystals to 2.2 eV for the Co-doped ones and 2.8-3.0 for the crystals doped with other TA impurities. The large red shift of the absorption edge for the Co-doped crystals has been attributed to the Co^{2+} - Co^+ photoionization transitions, while for the crystals, doped with other TA ions, the above-mentioned red shift has been assigned to defect states introduced by doping and formed to keep charge neutrality in the crystal.

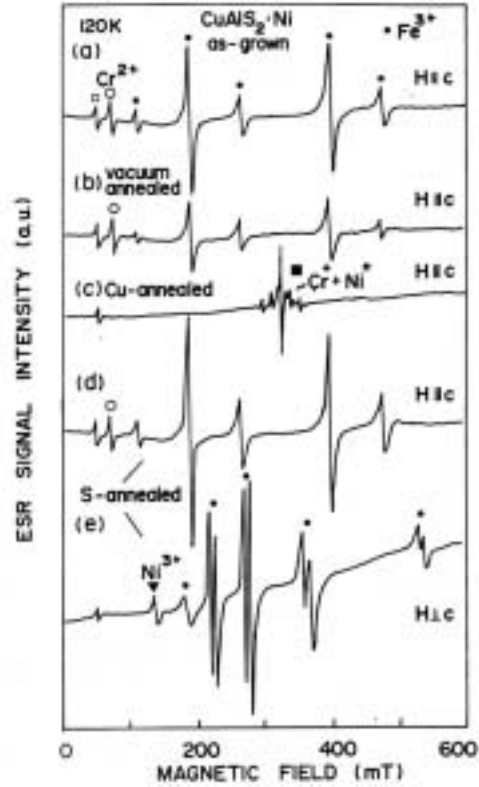2) The valence states ($i+$) of TA ions and the relative concentrations of these ions in each valence state are controlled by the position of the Fermi level in the band gap of the host crystal in relation to the demarcation levels of TA impurities $TA^{i+}/TA^{(i+1)+}$, the position of the Fermi level, in its turn, being dependent on the concentrations of electrically active native and extrinsic defects, including those formed by TA impurities (see Table 1 and Fig. 5 for the case of Cr impurity as an example).

3) It can be seen from Table 2 that the values of Dq for all TA ions in $CuAlS_2$ are larger and, to the contrary, the B values are smaller as compared with corresponding values of these parameters in ZnS. This result points out to a larger covalency of bonding in $CuAlS_2$.

5. Optical and ESR characterization of Mo-doped $CuAlS_2$

Figure 16 shows an ESR spectrum of $CuAlS_2$ single crystal doped with 0.5 wt% Mo at 20 K. [53] Three fine-structure lines which were observed at around 320 mT (g~2) is expected for an S=3/2 center $e.g.$ Mo^{3+} ion with $4d^3$ configuration. The lines are considered to be peculiar to the molybdenum ion, since no corresponding signal has been observed either in undoped crystals or in those doped with other 3d transition atoms, and the ESR signal at g~2 due to Mo^{3+} ions had been observed in the Al_2O_3 host. [54] The lines also show a slight anisotropy. If this dependence is originated from an anisotropy of the g-factors, the g value is obtained by the following equation,

$$g = (g_{//}^2 \cos^2\theta + g_\perp^2 \sin^2\theta)^{1/2} \qquad (1)$$

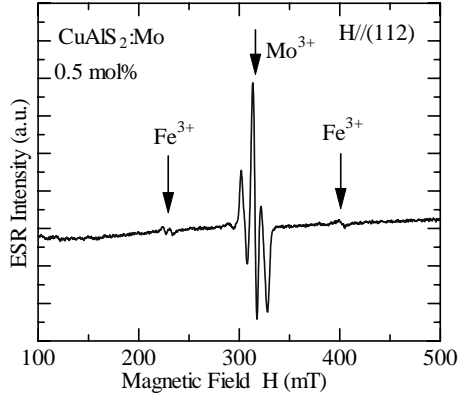Fig. 15 ESR spectra of the $CuAlS_2$ crystals, doped with Ni, as well as subsequently annealed in vacuum atmospheres. , , , and marks correspond to the signals from Fe^{3+}, Cr^{2+}, Ni^{3+}, Cr^++Ni^+ (two signals) ions and an unidentified impurity with a nearly isotropic g~11.95, respectively. [36]

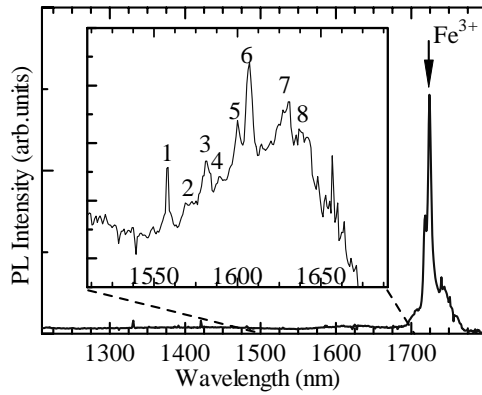Fig. 17. ESR spectrum of CuAlS$_2$:Mo (0.5 wt% Al site)at 20 K[53]

Fig. 18. PL spectrum of CuAl$_{0.995}$Mo$_{0.005}$S$_2$ at 6 K.[55]

where θ denotes the angle between the magnetic field H and the tetragonal c-axis of the crystal. From a fit of the above relation to the experimental data we obtain

$$g_{//} = 2.170\pm0.003,$$
$$g_{\perp} = 2.004\pm0.003.$$

The weighted mean g value is $g\cong2.059$, which is very close to the g value observed in the powdered sample. It is expected that the broad signal of the powdered sample is orientation average of the ESR lines having angular dependence in the single crystals. The analysis in terms of the spin-Hamiltonian is now underway.

If the trivalent molybdenum ion occupies a cubic cation-substitutional lattice site, its electronic ground state is the multiplet $^4T_1(^4F)$. In the theory, the $^4T_1(^4F)$ level of 4d^3 (S=3/2) configuration of Mo^{3+} splits into ^4E and $^4A_2$ terms by the tetragonal component of crystal field in chalcopyrite lattice. The ESR lines in the Mo doped crystal can be assigned to transitions between Zeeman-split levels of the $^4A_2$ state.

Figure 18 shows an infrared (IR) PL spectrum of CuAlS$_2$ doped with 0.5 wt% Mo at 6 K.[55] A fine-structure emission line was observed around 1600 nm (0.78 eV) in addition to a sharp strong emission line at 1724 nm (0.72 eV), the latter having been assigned to the ligand-field transition of Fe^{3+}.[45] The fine-structure emission line is thought to be peculiar to the molybdenum ion, since no corresponding emission has been ob-

served in CuAlS$_2$ crystals undoped or doped with other 3d transition atoms. The small line-width of the emission indicates that the transition is of the intra-center type. The PL emission consists of two zero phonon lines at 0.796 eV and 0.775 eV accompanied by phonon replicas was observed and was assigned to $^2T_1$ $^4T_1$ transition of 4d^3 of Mo^{3+}. In our previous work, the splitting of the excited state ($^4T_1$) of Co^{2+} in CuGaS$_2$ due to lower symmetry crystal field was determined to be 28.8 meV.[56] Since the anisotropy of the ESR signal is weak, the lower level may be $^4A_2$ without the orbital degeneracy. It is comparable with the value of the ground state separation between ^4E and $^4A_2$ levels of Mo^{3+} ion in CuAlS$_2$ determined to be 21 meV from the PL measurement.

Temperature-dependent PL measurements revealed the existence of thermal quenching above 60 K, whose activation energy was estimated to be about 4 meV. Figure 19 shows an Arrhenius plot of the temperature-dependence of PL and ESR signals due to Mo^{3+}. Both dependences show thermal quenching above 60 K, whose activation energy was estimated to be about 4 meV. These results also allow us to propose that the Mo^{3+} emission and the ESR signal result from the same center. The dependence of ESR signal of Fe^{3+} has the opposite slope of the quenching of the Mo^{3+} signals as shown in Fig. 19. The observed dependence indicates that the quenching process of the signals of Mo^{3+} ions is either directly or indirectly related to thermal ionization of Fe^{3+} ions. However, further studies are necessary to clarify the thermal process.
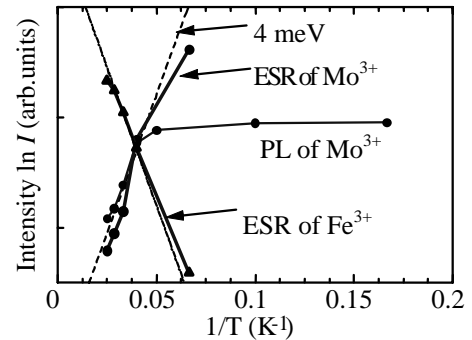

Fig. 19. Arrhenius plots of IR-PL and ESR signal intensity in CuAlS$_2$:Mo (0.5 wt% Al site) at 10 K.[53]

6. Chalcopyrite doped with rare earth ions

CuAlS$_2$ crystals doped with light RE elements (Ce, Pr, Nd, Sm and Eu) showed a yellow PL band as well as several blue or purple emissions. Both of these emissions have been observed also in undoped crystals and ascribed to so-called self-activated (SA) emission in undoped crystals. Neither sharp lines due to f-f transitions nor broad emission bands characteristic of d-f transitions were detected. We therefore concluded that these light RE ions could not be incorporated in CuAlS$_2$ crystals.

On the other hand, in crystals doped with heavy RE elements were observed sharp PL lines superposed on the broad yellow band. In Fig. 20 are illustrated PL spectra for wavelengths below 900 nm observed in crystals doped with Tb, Dy, Ho, Er and Tm. We will give brief discussion for each RE ion in the order of the filling of 4f-shell.
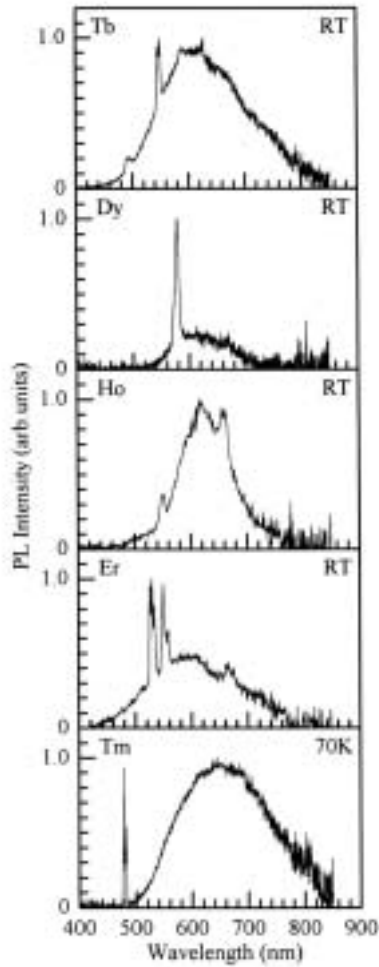
11

Fig. 20. PL spectra of $CuAlS_2$ single crystals doped with Tb^{3+}, Dy^{3+}, Ho^{3+}, Er^{3+} and Tm^{3+} ions.[10]

$Tb^{3+}(4f^8)$

Several lines were observed superposed on the yellow SA band.[57] All the sharp lines have been assigned to f-f transitions from a common excited state $^5D_4$ to several L-S coupling sublevels (J=6, 5, 4, 3) split from the ground multiplet ^5F. The most intensive line at 548 nm is regarded as a phonon-replica of $^5D_4$ → $^5F_5$ zero-phonon-line. The PL excitation (PLE) spectra for these lines showed a common peak at 380 nm (3.26 eV), which can be assigned to the transition from the lowest ground level to higher excited state $^5D_3$. These Tb-originated luminescence were hardly excited by across-the-gap transition.

$Dy^{3+}(4f^9)$

Only one sharp line was observed in the Dy-doped sample at 580 nm, which can be assigned to the transition $^4F_{9/2}$→$^6H_{13/2}$. We failed to measure an excitation spectrum for this line emission due to weakness of the emission intensity.[10]

$Ho^{3+}(4f^{10})$

Several lines superposed on the SA emission were observed in Ho-doped crystals. Lines observed at 656 nm, 635 nm, 620 nm, 590 nm and 551 nm can be assigned to $^5F_3$→$^5I_7$, $^5F_2$→$^5I_7$, $^3K_8$→$^5I_7$, $^5F_1$→$^5I_7$, $^5S_2$→$^5I_8$ intracenter transitions.[9]

$Er^{3+}(4f^{11})$

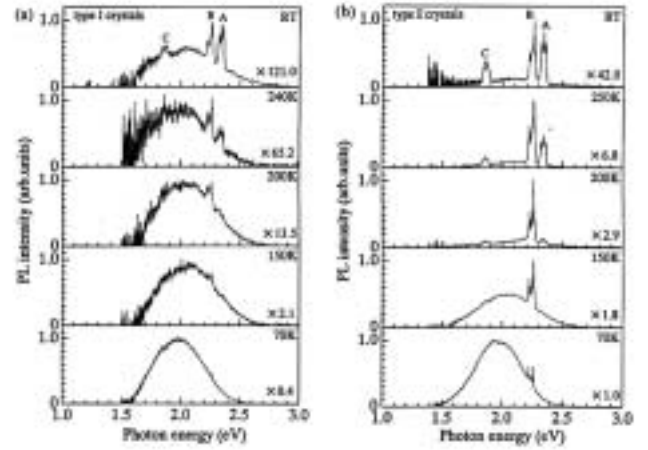Three distinct PL structures at 670 nm, 549 nm and 530 nm superposed on the broad SA emission band were observed and

Fig. 21. PL spectra for (a) type I (without intentional doping of Fe) and (b) type II (with 0.05mol% Fe doped) single crystals of Er-doped $CuAlS_2$ measured at different temperatures.

were assigned to f-f transitions $^4F_{9/2}$→$^4I_{15/2}$, $^4S_{3/2}$→$^4I_{15/2}$, $^2H_{11/2}$→$^4I_{15/2}$.[10] The color of the emission was yellow due to the presence of the strong SA emission.

As shown in Fig. 21, the broad band could be substantially suppressed by an intentional doping of very small amount of Fe impurity.[58] In this case the emission was pure green in color at room temperature. PLE spectra for these PL lines showed a common peak at 383 nm, which has been assigned to the transition from the ground state $^4I_{15/2}$ to the higher excited state $^4G_{11/2}$.

Infrared emission spectra between 1100 and 1800 nm measured at 20 K are illustrated in Fig. 22 in three different samples of Er-doped crystals; (a) *sample A* prepared from the starting material with molar composition ratio $CuAlS_2$:Er=0.95:0.05, (b) *sample B* with a starting composition of $Cu_{0.95}Er_{0.05}AlS_2$, and (c) *sample C* with a starting composition of $Cu_{0.95}Er_{0.05}Al_{0.9995}$ $Fe_{0.0005}S_2$. In samples B and C, well-known Er^{3+} emission lines at around 1540 nm could be obtained, which were assigned to the electronic transitions, $^4I_{13/2}$→$^4I_{15/2}$ between the LS-coupling terms of Er^{3+} ions having $4f^{11}$ electronic configuration. The strongest line peaks at 1536 nm. The sample C emitted not only
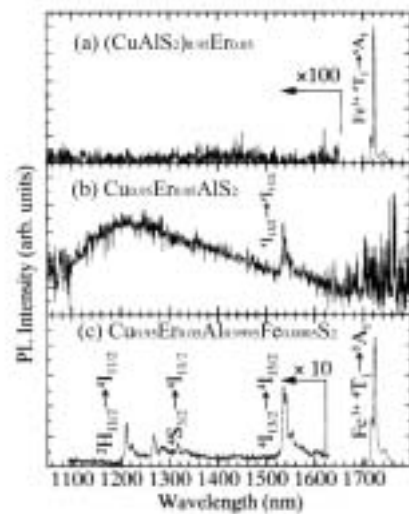

Fig. 22. Infrared PL spectra in three samples with different staring composition: (a) $(CuAlS_2)_{0.95}Er_{0.05}$, (b) $Cu_{0.95}Er_{0.05}AlS_2$ and (c) $Cu_{0.95}Er_{0.05}Al_{0.9995}Fe_{0.0005}S_2$ measured at 20 K.[11]

1540 nm lines but also the sharp lines at around 1210 nm and 1320 nm. These sharp emissions were tentatively assigned from Dieke's diagram to $^2H_{11/2}\rightarrow^4I_{11/2}$ and $^4S_{3/2}\rightarrow^4I_{11/2}$ intra 4f shell transition respectively. The levels of $^2H_{11/2}$ and $^4S_{3/2}$ are also the excited states of the Er^{3+} green emissions in the same crystals. A sharp strong emission at 1720 nm is due to the ligand field transition of Fe^{3+} ion that is typical impurity in $CuAlS_2$ crystal grown by CVT.[45] In the crystal B, the Fe^{3+}-related emission could not be detected. Since the emission is found to originate from the substitution of the copper site of $CuAlS_2$ by iron,[46] the disappearance of the emission in the crystal B suggests that substitution of Er atoms at Cu site induces substitution of most of Fe atoms at the Al sites. The similar effect of Fe-substitution was also observed in Mo-doped $CuAlS_2$ crystals.[55] It is expected that the Fe ion at Al site becomes divalent to compensate the broken charge neutrality by putting the Er^{3+} at the Cu site. Not only an existence of Fe^{3+} on Cu site was confirmed by the IR-emission, but also an existence of Fe^{2+} ions was confirmed by IR absorption.[58] This fact indicates that co-doping with Fe decreases the copper composition in the crystal C, resulting in an increased occupation of Er on Cu-site.

$Tm^{3+}(4f^{12})$

At room temperature, only one near infrared (NIR) PL line is seen at 800 nm (1.55 eV) overlapped on the broad SA emission band. As temperature is decreased, a blue emission line appears at 477 nm (2.6 eV).[59] At 70 K, the NIR line is buried into the SA-band and the blue emission becomes dominant. It should be noted that the assignment of the observed emission lines to the f-f transitions between energy levels in the Dieke diagram is not unique. The IR emission can be assigned either to $^1G_4\rightarrow^3H_5$ or to $^3F_4\rightarrow^3H_6$ (ground state) f-f transitions, while the blue emission may originate from either $^1G_4\rightarrow^3H_6$ or $^1D_2\rightarrow^3H_5$ transitions in the $4f^{12}$ manifold of the Tm^{3+} ion. These emissions were excited by a broad PLE band peaked at 400 nm, which have been tentatively ascribed to the charge-transfer transition from the ligand p-orbitals to 4f orbitals. Since $^1D_2$ state is located above the PLE band, assignment of the blue emission to $^1D_2\rightarrow^3H_5$ can be ruled out. Therefore, the blue emission is safely attributed to $^1G_4\rightarrow^3H_6$ transition. Taking into account the different temperature dependence, we consider that the excited state for the IR emission should be different from that of the blue emission. We therefore assign the 1.55-eV NIR emission to $^3F_4\rightarrow^3H_6$.
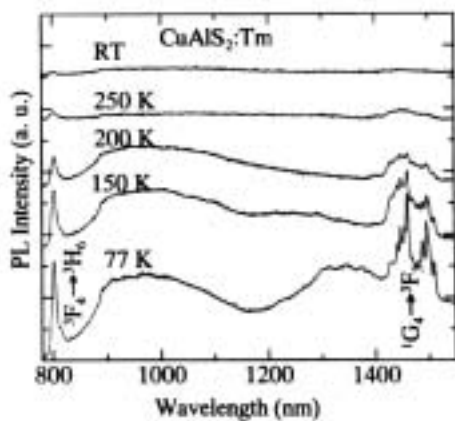

Fig. 23. Infrared PL spectrum in a $CuAlS_2$ single crystal doped with Tm. [60]

The IR-PL spectrum in a Tm-doped crystal of $CuAlS_2$ at 20 K is shown in Fig. 23.[60] Two broad emission bands were observed around 880 nm and 1340 nm, as well as a series of two sharp emission lines with peaks at 1136 nm and at around 1500 nm. These broad bands have been observed in $CuAlS_2$ crystals doped with high concentration of ions relatively large in size, and tentatively ascribed to some emission centers inherent to the host $CuAlS_2$. The three sharp emission lines observed at 1136 nm, 1460 nm and 1500 nm may be associated with f-f transitions in Tm^{3+} ions. Based on the Dieke diagram the PL line at 1136 nm can be assigned to either one of the f-f transitions, $^1G_4\rightarrow^3F_4$, $^3F_3\rightarrow^3H_4$ and $^3H_5\rightarrow^3H_6$ between the LS-coupling terms of Tm^{3+}. The fine structure emission lines at 1460 and 1500 nm were tentatively assigned to $^1G_4\rightarrow^3F_3$ transitions, which shares the same excited term $^1G_4$ with the blue emission due to $^1G_4\rightarrow^3H_6$ transition at 477 nm, since both show a quite similar temperature quenching.
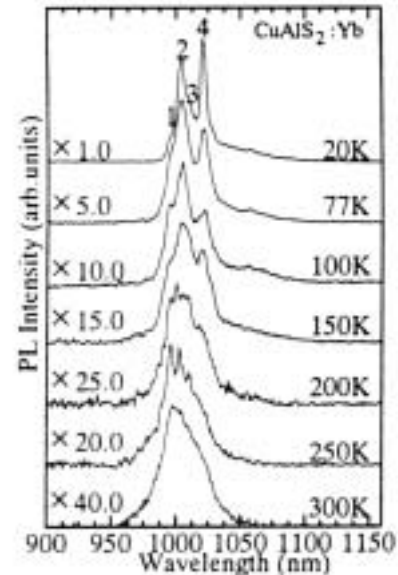

Fig. 24. Temperature dependence of IR-PL spectra of Yb-doped $CuAlS_2$.[60]

$Yb^{3+}(4f^{13})$

Temperature dependence of IR-PL in Yb-doped $CuAlS_2$ is shown in Fig. 24.[60] At 20 K only one PL band with fine structure is observed around 1000 nm. Using Dieke diagram this emission has been assigned to f-f transition of Yb^{3+}. For the free Yb^{3+} ion only one transition $^2F_{5/2}$ $^2F_{7/2}$ between LS coupling states is expected. Overall temperature dependence of the Yb^{3+}-emission is quite similar to that of the Tm^{3+}. However, since thermal quenching of the Yb^{3+} PL is not so rapid as Tm^{3+}, the emission can be observed still at room temperature. We can also observe thermal broadening of the Yb^{3+}-related emission.

The temperature dependence was explained in terms of the three-center Auger recombination (TCAR) model proposed by Godlewski et al to explain the similar behavior observed in ZnS:Yb.[61] This model requires charge transferred state (CTS) as an intermediate state. The energy position of CTS for Yb^{3+} can be estimated from that of the CTS for Tm^{3+} as 1.8-2.0eV, by assuming the same energy difference between CTS for Yb and Tm in oxides is applied to our material. The PLE spectrum showed a broad band with a peak at 620 nm (2.0 eV). At the

same energy region was observed a broad emission band ascribed to the D-A pair emission. (1) CTS of Yb^{3+} is excited by the D-A pair emission energy bringing one hole out of 4f shell, resulting in Yb^{2+}. (2) The hole brought out is bound strongly by Yb^{2+}, thus Yb-bound exciton (BE) is formed. (3) The BE nonradiatively recombines, by which a hole in 4f shell is excited, then $^2F_{5/2}$ $^2F_{7/2}$ transition occurs.

Summary of 4f ions

The PL lines and their assignment are tabulated in Table 4. Ionic radii of RE ions decrease with atomic number, this phenomenon having been well known as lantanide contraction. It seems that there is a certain critical radius of RE ions to be incorporated into the $CuAlS_2$ crystal lattice. Since tetrahedral covalent bond radius (1.26 Å), as well as ionic radius (0.5 Å), is smaller than corresponding values (1.35 Å and 0.68 Å) of Cu, we believe RE ions prefer to substitute the Cu atom, charge neutrality being satisfied either by an introduction of cation vacancy or by a reduction in valency of impurity Fe ion at Al site from trivalent to divalent. Thus the covalent radius of Cu may determine critical size.

Table 4. Photoluminescence in RE-doped $CuAlS_2$

RE	Emission line position		Assignment	PLE peak(eV)
	Energy (eV)	Wave-length (nm)		
Tb^{3+}	1.99	621	$^5D_4\rightarrow^7F_3$	3.26 $^7F_6\rightarrow^5D_3$
	2.11	587	$^5D_4\rightarrow^7F_4$	
	2.262	548	$^5D_4\rightarrow^7F_5$	
	2.278	544	$^5D_4\rightarrow^7F_5$	
	2.532	490	$^5D_4\rightarrow^7F_6$	
Dy^{3+}	2.14	580	$^4F_{9/2}\rightarrow^6H_{13/2}$	
Ho^{3+}	1.89	656	$^5F_3\rightarrow^5I_7$	
	1.95	635	$^5F_2\rightarrow^5I_7$	
	2.00	620	$^3K_8\rightarrow^5I_7$	
	2.10	290	$^5F_1\rightarrow^5I_7$	
	2.25	551	$^5S_2\rightarrow^5I_7$	
Er^{3+}	0.805	1540	$^2H_{13/2}\rightarrow^4I_{15/2}$	3.24 $^4I_{15/2}\rightarrow^4G_{11/2}$
	0.939	1320	$^4S_{3/2}\rightarrow^4I_{11/2}$	
	1.024	1210	$^2H_{11/2}\rightarrow^4I_{11/2}$	
	1.85	670	$^4F_{9/2}\rightarrow^4I_{15/2}$	
	2.26	549	$^4S_{3/2}\rightarrow^4I_{15/2}$	
	2.34	550	$^2H_{11/2}\rightarrow^4I_{15/2}$	
Tm^{3+}	0.827	1500	$^1G_4\rightarrow^3F_3$	3.10 CTS
	0.849	1460		
	1.092	1136	$^3F_3\rightarrow^3H_4$ or $^3H_5\rightarrow^3H_6$	
	1.55	800	$^3F_4\rightarrow^3H_6$	
	2.60	477	$^1G_4\rightarrow^3H_6$	
Yb^{3+}	1.21	1025	$^2F_{5/2}\rightarrow^2F_{7/2}$	2.0 CTS
	1.23	1008		

7. II-IV-V$_2$ compounds doped with Mn

The ternary compound family with common formula II-IV-V$_2$ that was developed in early works of Goryunova as a group of crystal-chemical analogs of III-V compounds has been investigated quite intensively for last 40 years.[62] A series of materials from this family attracts attention as materials for new functionality devices such as nonlinear optical elements (ZnGeP$_2$, CdGeAs$_2$), polarization sensitive strong photoresponse devices (CdSnP$_2$, CdGeP$_2$, CdSiAs$_2$). Wide possibilities in heteroepitaxy of solid solutions with III-V compounds are also promising for device applications.

Contrary to I-III-VI$_2$ compounds, only a few studies have been carried out on the effect of transition-atom doping in II-IV-V$_2$ family materials of ternary compounds. Small concentration of Mn as a dopant have been examined, but so far no noticeable magnetic and optical properties are reported.[63] Since this series contains the group II element as their constituent element, considerable amount of divalent transition ions are expected to be introduced, just like Mn in II-VI compounds. We therefore started to incorporate Mn into II-IV-V$_2$ compounds.

A single crystal of CdGeP$_2$, which has been grown at the Ioffe Institute by directional crystallization, was used as a host material. The flat-parallel crystal plate showed nearly rectangular shape with size of 3×5 mm^2. Thin Mn layer of about 30 nm in thickness was deposited at 390°C on the CdGeP$_2$ crystal in a MBE chamber using a Knudsen cell for evaporation of Mn source, followed by the thermal treatment at about 500°C for 30 minutes.[8]

Taking into account the ionic radii of Mn, Cd and Ge, we assume most of the Mn occupies the divalent Cd-site. The Mn/Cd ratio analyzed by EDX at the surface reaches 53.4% and drops rapidly with depth, the value being 12.7% at 0.6 μm and 0.9% at 2.5 μm. The average Mn/Cd ratio is determined as 20% for effective thickness 0.5 μm.[8]

Any traces of extraneous phases could not be found in conventional XRD measurement on the grown layer. We also found that the crystal structure of the grown layer does not strongly differ from the substrate CdGeP$_2$, except for the top-most surface in which a texture formation is confirmed.

The PL spectrum of CdMnGeP$_2$ is plotted in Fig. 25, together with that of undoped CdGeP$_2$. It shows a broad emission band between 1.6 and 3.6 eV with a peak at 3.24 eV, suggesting that the new material CdMnGeP$_2$ grown on the crystal surface of the CdGeP$_2$ single crystal is also a semiconductor with an enlarged energy gap *Eg* relative to the gap (1.83 eV) of the host semiconductor. The distribution of the PL energy may correspond to the distribution of *Eg* from 1.8 eV of the host to 3.5 eV of the top surface layer. This fact can be associated with the distribution of Mn/Cd ratio from nearly zero (0.9%) at 2.5μm to 53% at surface.

The magnetization curve measured at room temperature is shown in Fig. 26.[64] The curve is composed of diamagnetic and ferromagnetic components. The former may be attributed to the host substrate and the latter to the new DMS layer. The ferromagnetic component shows a well-defined hysteresis loop with
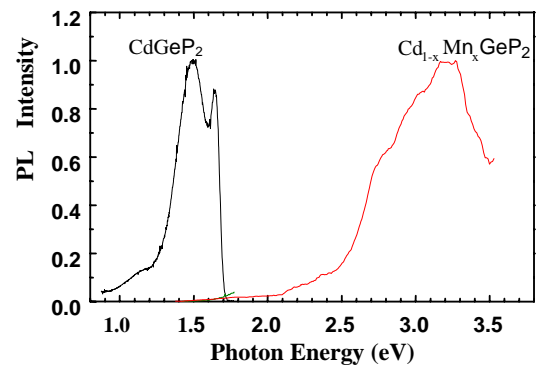

Fig. 25. Photoluminescence spectra of Cd$_{1-x}$Mn$_x$GeP$_2$ and CdGeP$_2$ crystals measured at 20 K.[8]

the saturation field H_s of 2 kOe and coercivity H_c of about 0.5 kOe. The result clearly suggests that Curie temperature T_c is higher than room temperature. The magnetic moment estimated from the saturation magnetization was 1.03 μ_B per Mn atom provided that all the Mn atoms deposited are contributing to the magnetization. Temperature dependence of the remanent magnetization could be fitted by the molecular field theory with S=1/2, from which T_c was determined to be 320 K.[64] It is recently found that the material shows ferromagnetic behavior above Tc, even at 420K.

AFM and MFM images (8 μm×8 μm) on the surface of the CdMnGeP$_2$ at the remanent magnetization state were measured at room temperature. The MFM image clearly shows the stripe-shaped magnetic domain structure, supporting existence of magnetization at the surface of the DMS layer.

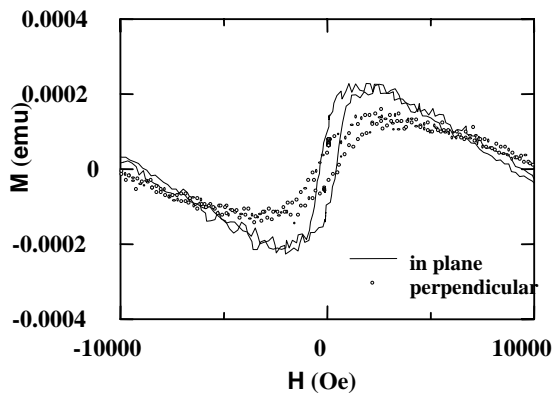The magnetooptical Kerr ellipticity η_K was measured at room

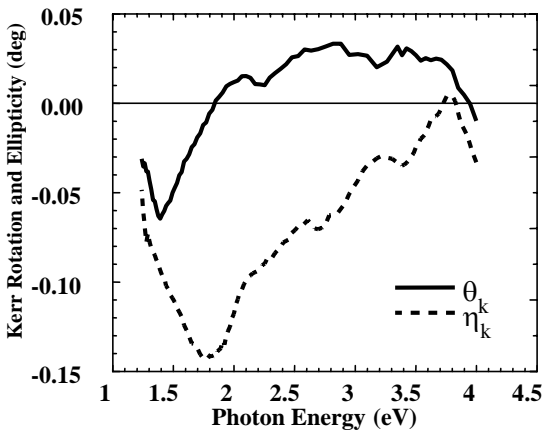Fig. 26. Magnetization curve of the CdMnGeP$_2$ layer at 298 K.[64]

Fig. 27. Spectra of magneto-optical Kerr rotation θ_K and Kerr ellipticity in the CdMnGeP$_2$ layer at 300 K.

temperature for photon energies between 1.2 and 4.0 eV.[65] As shown in Fig. 27, the magneto-optical effect is relatively weak with the absolute value of η_K no greater than 0.14°. Specific Faraday rotation was estimated to be as large as 50,000 deg/cm assuming that dielectric constant is the same as the host material.[65]

Recently, we have found that Mn can also be easily incorporated into ZnGeP$_2$ single crystals. In this case we deposited Mn on the polished surface of ZnGeP$_2$ crystal at substrate temperature of 400°C. Real-time RHEED observation revealed that diffraction spots due to chalcopyrite structure observed before

deposition becomes streaky 30 s after beginning of Mn deposition but the spot is recovered before 1000 s. The Mn-deposited layer was found to exhibit a ferromagnetic magnetization curve up to 350 K as shown in Fig. 28. No traces of extraneous compounds were found by an accurate XRD analysis.

Recently Kim et al. succeeded in fabrication of Mn-doped ZnGeAs$_2$ by MBE and observed ferromagnetism with T_c higher than room temperature.[66]

These results may be explained by the higher solubility of Mn atoms in the II-IV-V$_2$ than in the III-V compounds. Therefore we believe ferromagnetism can occur commonly in Mn-doped II-IV-V$_2$ semiconductors.

Recently ab-initio calculation were carried out in Cd$_{1-x}$Mn$_x$GeP$_2$ with x=0.25, 0.5 and 1.0, which could not explain ferromagnetism, but make antiferromagnetic states stable if Mn occupies the group II element.[67] On the contrary, Akai showed that ordering of Mn and introduction of defects could explain
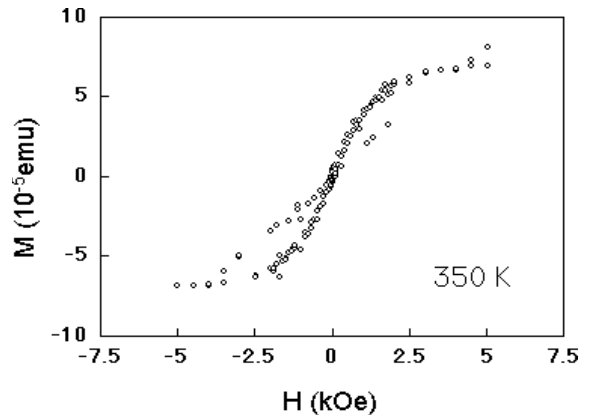
Fig. 28 Magnetization curve of the ZnGeP$_2$ layer at 350 K measured using SQUID magnetometer.

ferromagnetism in this material.[68] In ternary compounds, presence of intrinsic defect should be taken into account. Zunger et al. have recently shown theoretically that Mn-doped CdGeP$_2$ could be ferromagnetic if one assumes the interaction of Mn with hole-producing intrinsic defects in the host semiconductor.[69] Further experimental effort is necessary to clarify detailed structure of this new material family.

8. Conclusion

Physical properties of chalcopyrite semiconductors doped with transition and rare earth elements have been reviewed. It is found that valence state of transition atoms can be altered by an appropriate annealing process, which introduces intrinsic donors or acceptors resulting in the shift of Fermi level relative to the demarcation levels delineating the different valence states associated with the individual transition element.

Electronic states of the transition atom are different in character corresponding to the site, which it occupies. Light rare earth elements can be incorporated in I-III-VI$_2$ semiconductors to become luminescence centers. Co-doping of Fe is found to be effective to suppress SA emission and enhance the emission inherent to rare earth elements.

It is recently clarified that the solubility of Mn is higher in II-IV-V$_2$ chalcopyrite compounds than in III-V semiconductors, resulting in an appearance of room temperature ferromagnetism in these materials. Transition atom-doped chalcopyrite crystals seem to have further potentiality for future materials researches.

1. J.L. Shay and J.H. Wernick: *Ternary Chalcopyrite Compounds* (Pergamon Press, Oxford, 1975)
2. K. Sato, H. Tsunoda and T. Teranishi: *Proc. 7th Int. Conf. Ternary & Multinary Compounds, Snowmass, CO., 1986* (Mater. Res. Soc., Pittsburgh, 1987) p. 459.
3. P. C. Donohue, J. D. Bierlein, J. E. Hanlon and H. S. Jarett: J. Electrochem. Soc. 121 (1974) 829.
4. H. J. von Bardeleben, A. Goltzene and C. Schwab, *Proc. 2nd Int. Conf. Ternary & Multinary Compounds, Strasbourg, 1975,* J. Physique 36 (1975) Suppl. 9, C3, p. 47.
5. K. Sato, I. Aksenov, N. Nishikawa and T. Kai: *Proc. 9th Int. Conf. Ternary and Multinary Compounds, Yokohama, 1993,* Jpn. J. Appl. Phys. **32** (1993) Suppl. 32-3, 481
6. K. Sato: *Recent Advances in Magnetism of Transition Metal Compounds, edited by A. Kotani and N. Suzuki* (World Scientific, 1993) p. 127
7. T. Ohgoh, Y. Kudo and K. Sato: *Proc. 9th Int. Conf. Ternary and Multinary Compounds, Yokohama, 1993,* Jpn. J. Appl. Phys. 32 (1993) Suppl. 32-3, 608.
8. G.A. Medvedkin, T. Ishibashi, T. Nishi, K. Hayata, Y. Hasegawa and K. Sato: Jpn. J. Appl. Phys. **39** (2000) L949.
9. T. Ohgoh, Y. Kudo and K. Sato: *Proc. 9th Int. Conf. Ternary and Multinary Compounds, Yokohama, 1993,* Jpn. J. Appl. Phys. 32 (1993) Suppl. 32-3, 608.
10. K. Sato, Y. Kimura, K. Shimizu, T. Ohgoh and Y. Kudo: *Proc. 10th Int. Conf. Ternary and Multinary Compounds,Stuttgart, 1995,* Cryst. Res. Technol. **31**, Suppl. (1996) 713.
11. T. Nishi, Y. Kimura and K. Sato: J. Luminesc. **87-88** (2000) 1105.
12. K. Kondo, T. Teranishi and K. Sato: J. Phys. Soc. Jpn. 36 (1974) 311.
13. T. Kambara,: J. Phys. Soc. Jpn. 36 (1974) 1625.
14. I. Aksenov, Y. Kudo and K. Sato: Jpn. J. Appl. Phys. **31** (1992) L145
15. S. Endo, T. Irie, and H. Nakanishi: Solar Cells **16** (1986) 1
16. H. Miyake: Recent Dev. Bulk Cryst. Growth **9** (1998) 271
17. K. Sato: Jpn. J. Appl. Phys. **20** (1981) 2403.
18. I. Aksenov and K. Sato: Appl. Phys. Lett. **61** (1992) 1063.
19. I. Aksenov, I. Gulakov, V. Lipnitskii, A. Lukomskii and L. Makovetskaya: Phys. Status Solidi a **115** (1989) K113.
20. T. Teranishi, K. Sato and K. Kondo: J. Phys. Soc. Jpn. 36 (1974) 1618.
21. R. Pappalardo and R.E. Dietz: Phys. Rev. **123** (1961) 1188.
22. J. Schneider, A. Räuber and G. Brandt: J. Phys. Chem. Solids **34** (1973) 443.
23. G. Brandt, A. Räuber and J. Schneider: Solid State Commun. **12** (1973) 481.
24. K. Morigaki: J. Phys. Soc. Jpn. **19** (1964) 187.
25. M.de Wit, A. R. Reinberg, W.C. Holton and T.L. Estle: Bull. Am. Phys. Soc. **10** (1965) 329.
26. X. J. Li, Y. Kudo, S. Matsuda, I. Aksenov and K. Sato: Jpn. J. Appl. Phys. **31** (1992) L303.
27. U. Kaufmann: Phys. Rev. **B11** (1975) 2478.
28. G.L. Troeger, R.N. Rogers and H.M. Kasper: J. Phys. C. **9** (1976) L73.
29. I. Aksenov and K. Sato: Jpn. J. Appl. Phys. **31** (1992) 2352.
30. R.S. Title: Phys. Rev. **131** (1963) 623.
31. J.W. Allen: Physica **29** (1963) 764.
32. K. Sato, M. Morita, S. Okamoto, S. Morita, T. Kambara, K. Gondaira and H. Takenoshita: *Proc. 6th Int. Conf. Ternary & Multinary Compounds, Caracas, 1984,* Prog. Cryst. Growth Charact. **10** (1985) 311.
33. D.S. McClure: J. Chem. Phys. **39** (1963) 2850.
34. I.Aksenov, T. Kai, N. Nishikawa and K. Sato: Jpn. J. Appl. Phys. **32** (1993) L516.
35. H. Weakliem: J. Chem. Phys. **36** (1962) 2117.
36. I.Aksenov, T. Kai, N. Nishikawa and K. Sato: Jpn. J. Appl. Phys. **32** (1993) 3391.
37. U. Kaufmann: Solid State Commun. **19** (1976) 213.
38. U. Kaufmann, A. Räuber, and J. Schneider: Solid State Commun. **15** (1974) 1881.
39. I.Aksenov and K. Sato: Jpn. J. Appl. Phys. **31** (1992) L527.
40. U. Kaufmann, A. Räuber, and J. Schneider: J. Phys. C: Solid State Physics **8** (1975) L381.
41. H.H. Woodbury and G.H. Ludwig: Bull. Am. Phys. Soc. **6** (1961) 118.
42. K. Sato, K. Ishii, K. Watanabe and K. Ohe: Jpn. J. Appl. Phys. **30** (1991) 307.
43. K. Sato, K. Ishii, K. Tanaka, S. Matsuda and S. Mizukawa: *Electroluminescence, eds. S. Shionoya and H. Kobayashi* (Springer, Berlin, 1989) p.390.
44. K. Tanaka, Y. Kimura, S. Okamoto, Y. Inoue and K. Sato: Jpn. J. Appl. Phys. **37** (1998) 3350.
45. K. Sato and T. Teranishi: J. Phys. Soc. Jpn. **37** (1974) 415.
46. K. Sato, K. Tanaka, K. Ishii, and S. Matsuda: J. Cryst. Growth **99** (1990) 772.
47. K. Sato, I. Aksenov, N. Nishikawa, T. Shinzato and H. Nakanishi: Cryst. Res. Technol. **31** S (1996) 593.
48. E. E. Vogel, O.M. Mualin, A. de Orue and J. Rivera-Iratchet: Phys. Rev. **B 44** (1991) 1579.
49. K. Sato, Y. Katsumata and T. Nishi: *Proc. 12th Int. Conf. Ternary and Multinary Compounds, Hsinchu, 2000,* Jpn. J. Appl. Phys. **39** (2000) Suppl. 39-1, 405
50. K. Sato, N. Nishikawa, I. Aksenov, T. Shinzato and H. Nakanishi: Jpn. J. Appl. Phys. **35** (1996) 2061.
51. T. Nishi, G.A. Medvedkin, Y. Katsumata, K. Sato and H. Miyake: Jpn. J. Appl. Phys. **40** (2001) 59.
52. H. J. von Bardeleben, C. Schwab and A. Goltzene: Phys. Lett. **A 51** (1975) 460.
53. T. Nishi, Y. Katsumata and K. Sato: *Proc. 12th Int. Conf. Ternary & Multinary Compounds, Hsinchu, March 2000,* Jpn. J. Appl. Phys. **39** (2000) Suppl. 39-1, p.106.
54. E. G. Sharoyan, O. S. Torosyan, E. A. Markosyan and V. T. Gabrielyan: Phys. Status Solidi (b) **65** (1974) 773.
55. T. Nishi, N. Ishibashi, Y. Katsumata and K. Sato: Jpn. J. Appl. Phys. **38** (1999) 683.
56. K. Suzuki, T. Kambara K. Gondaira, K. Sato, K. Kondo, and T. Teranishi: J. Phys. Soc. Jpn. **39** (1973) 1310.
57. Y. Kudo, N. Kojima, Y. Takada, I. Aksenov and K. Sato: Jpn. J. Appl. Phys. **31** (1992) L663.
58. Y. Kimura, T. Ohgoh, I. Aksenov and K. Sato: Jpn. J. Appl. Phys. **35** (1996) 3904.
59. T. Ohgoh, I. Aksenov, Y. Kudo and K. Sato: Jpn. J. Appl. Phys. **33** (1994) 962.
60. T. Nishi, Y. Kimura, K. Shimizu and K. Sato: *Proc. 11th Int. Conf. Ternary and Multinary Compounds, Salford September 1997*, Inst. Phys. Conf. Ser. No. **152**, 1998, p.405.
61. M. Godlewski, K. Swiatek, A. Suchocki and J.M. Langer: J. Luminesc. **48&49** (1991) 23.
62. N.A. Goryunova: *Complex diamond-like semiconductors* (Soviet Radio, Moscow, 1968)
63. Landolt-Börnstein: *Semiconductors: Physics of Ternary Compounds*, ed. O. Madelung (Springer, Berlin, 1985) vol. 17h.

64. K. Sato, G.A. Medvedkin, T. Ishibashi, T. Nishi, R. Misawa, K. Yonomitsu and K. Hirose: J. Magn. Soc. Jpn. **25** (2001) 735.(In Japanese)
65. K. Sato, G.A. Medvedkin, K. Hayata, Y. Hasegawa, T. Nishi, R. Misawa and T. Ishibashi: *Proc. Joint Magneto-optical Recording Int. Conf./ Asia Pacific Data Storage Conference 2000, Nagoya, October, 2001,* J. Magn. Soc. Jpn. **25** (2001) 283.
66. Y. Kim, B. Choi, S. Cho, A. DiVenere, G. K. Wong, J. B. Ketterson, J. R. Meyer: *Extended Abstract APS Conf. Seattle, March 14, 2001*, Q25.001.
67. Y.J. Zhao, W.T. Geng, A.J. Freeman and T. Oguchi: Phys Rev. B **63** (2001) 201202(R).
68. H. Akai: Private Communication.
69. P. Mahadevan and A. Zunger: Private Communication